Pyrite chemistry: A new window into Au-Te ore-forming processes in alkaline epithermal districts, Cripple Creek, Colorado

Manuel Keith[a, b, c *], Daniel J. Smith[c], Keiran Doyle[c, d], David A. Holwell[c], Gawen R. T. Jenkin[c], Tiffany L. Barry[c], Joseph Becker[e], Jason Rampe[e]

[a] *GeoZentrum Nordbayern, Friedrich-Alexander-Universität Erlangen-Nürnberg, 91054 Erlangen, Germany*

[b] *Technische Universität Berlin, Institut für Angewandte Geowissenschaften, 10587 Berlin, Germany*

[c] *University of Leicester, School of Geography, Geology and the Environment, Leicester, LE1 7RH, UK*

[d] *University of Exeter, Camborne School of Mines, Penryn, TR10 9FE, UK*

[e] *Newmont Mining Corporation, Victor, CO 80860, USA*

[*] *Corresponding author: GeoZentrum Nordbayern, Friedrich-Alexander-Universität Erlangen-Nürnberg, Schlossgarten 5, 91054 Erlangen, Germany,*

Email address: manuel.keith@fau.de

Abstract

Tellurium has a wide variety of applications, most importantly in the solar energy industry and is eco-toxicologically significant; however, the magmatic-hydrothermal processes causing the pronounced Te enrichment together with Au in some epithermal districts are still poorly constrained. Hydrothermal and alkaline magmatic activity in post-subduction

environments are suggested to be a critical component in the evolution of this Te-rich sub-class of low-sulfidation epithermal deposits. Cripple Creek represents an example for a world-class low-sulfidation epithermal Au-Te anomaly in the continental crust. This area represents a natural laboratory to investigate the processes of ore-formation and Au-Te enrichment in alkaline igneous rock-hosted epithermal systems.

Here, we present the first micro-analytical approach that combines petrographic observations with *in situ* LA-ICP-MS analyses and trace element mapping to define the key ore-forming processes of Au and Te in the Cripple Creek epithermal complex. Two main styles of mineralization can be distinguished: (1) low-grade Au disseminated pyrite-rich ores in the permeable brecciated host rocks and (2) high-grade quartz-fluorite veins rich in calaverite ($AuTe_2$), coloradoite (HgTe), petzite (Ag_3AuTe_2), altaite (PbTe) and native Au.

Pyrite trace element mapping revealed distinct variations and decoupling of elements (Au-Te) and element pairs (Au-As vs. Co-Ni) within and between different sites in the epithermal district. This is reflected by the concentric/growth zoning of these elements in pyrite that were interpreted to be caused by fluid boiling associated with the deposition of the low-grade disseminated host rock ores at temperatures between 220 and 350°C leading to the precipitation of Au, As, Co and Ni from the liquid phase and the preferential partitioning of Te into the vapor phase. The subsequent condensation of the Te-rich vapors in metal-bearing meteoric waters led to the Te precipitation being decoupled from Au in the low-grade ores.

The high-grade Au-Te mineralization was likely initiated by the influx of magmatically derived oxidized fluids. Subsequently, fluid temperatures dropped due to mixing with meteoric waters resulting in fluid boiling under low pressure conditions at shallower crustal levels (<1000 m) compared to the low-grade ores. Elevated fO_2 minimized the loss of Te to the vapor phase and the strong boiling conditions at lower fluid temperatures (105 to 200°C) caused the contemporaneous precipitation of Au and Te in the high-grade veins.

1 Introduction

Alkaline igneous rock-hosted epithermal systems are among the largest epithermal Au-Ag-Te deposits in the world. Prominent examples include the world-class Au-Ag deposits of Cripple Creek (Colorado), Porgera and Ladolam (Papua New Guinea) and Vatukoula (Fiji) (Richards and Kerrich, 1993; Kelley et al., 1998; Pals et al., 2003). These deposits are commonly classified as an "alkaline-hosted" or "gold-telluride" sub-group of low-sulfidation epithermal systems that are characterized by: (1) the lack of acid alteration in the presence of hydrothermal carbonate and K-feldspar, (2) the relatively quartz-poor alteration assemblages, (3) abundant telluride mineralization and (4) frequent association with alkaline igneous host rocks (Jensen and Barton, 2000; Sillitoe, 2002; Kelley and Spry, 2016).

Despite its low crustal abundance of 5 ppb (Wedepohl, 1995), Te can be enriched in alkaline-hosted epithermal deposits reaching concentrations >0.5 wt. % in the bulk ore (Kelley and Spry, 2016). Although this has been recognized for decades, the processes responsible for the Te-enrichment and association of Te with Au- and Ag-rich ores are still poorly constrained (Thompson et al., 1985; Kelley et al., 1998; Cooke and McPhail, 2001; Grundler et al., 2013; Smith et al., 2017). Low-sulfidation epithermal deposits are distributed globally, but their alkaline-hosted Te-rich endmembers only occur in post-subduction or back-arc settings; typically in a transitional stress regime between compression and extension (Jensen and Barton, 2000; Kelley and Spry, 2016). The processes causing the Te-enrichment in these specific tectonic environments are interpreted to be the result of complex and multi-stage magmatic-hydrothermal processes (Pals and Spry, 2003; Pals et al., 2003; Richards 2011; Kelley and Spry, 2016; Keith et al., 2018a2). These include the formation of silica-undersaturated alkaline igneous rocks (>40 to <80 wt. % SiO_2; up to 16 wt. % $Na_2O + K_2O$) from small volumes of oxidized and volatile-rich low degree partial melts of subduction zone modified material, which seems to be an essential component for the epithermal deposition of Au-Te ores (Jensen and

Barton, 2000; Kelley and Ludington, 2002; Holwell et al., 2019). In multi-stage alkaline-hosted epithermal systems, the Au-Te mineralization usually occurs during late stages of magmatic activity, characterized by the interaction of magmatic and meteoric fluids along structurally controlled fluid pathways leading to the typical enrichment of Te and Au in high-grade vein-type ores (Jensen and Barton, 2000; Ronacher et al., 2004; Spry and Scherbarth, 2006; Kelley and Spry, 2016).

Ore-forming fluids in alkaline-hosted Au-Te-rich environments are typically of lower temperature (<250 to 300°C), neutral to alkaline pH, low salinity and higher oxidation states (stability field of hematite and pyrite) enhancing the mobilization and transportation of Te and Au to the site of metal deposition (Cook et al., 2009b; Grundler et al., 2013; Smith et al., 2017). Various hydrothermal processes have been considered to be important for the precipitation of Te-rich ores by causing a destabilization of the Te-bearing complexes in ore-forming fluids including: (1) phase separation and conductive cooling along the boiling curve, (2) vapor condensation, (3) fluid mixing and (4) fluid-wall rock interaction (Cooke and McPhail, 2001; Ciobanu et al., 2006; Cook et al., 2009b; Keith et al., 2018a). For instance, experimental and empirical data emphasize that element partitioning between vapor (e.g., Te, Hg, As) and liquid (e.g., Zn, Fe, Cu, Ag, Au) by phase separation is a critical process for metal and metalloid fractionation and precipitation at variable crustal depth (Cooke and McPhail, 2001; Pokrovski et al., 2002; Grundler et al., 2013; Pokrovski et al., 2013; Tardani et al., 2017; Zajacz et al., 2017; Román et al., 2019).

Here, we present trace element data in pyrite from the world-class Cripple Creek alkaline-hosted epithermal Au-Te deposit. We use pyrite in particular, since it is a common constituent in the Earth's crust and incorporates many trace metals in detectable amounts either in solid solution by Fe and S substitution or as micro- to nano-sized inclusions (Pals et al., 2003; Reich et al., 2005, 2013; Deditius et al., 2014; Gregory et al., 2014, 2015; Keith et al.,

2016a, b; Deditius and Reich, 2016; Keith et al., 2018a; Martin et al., 2019; Pokrovski et al., 2019). Tellurium and Au are typically enriched in As-rich (arsenian) pyrite sometimes reaching economic concentrations (Kesler et al., 2007; Deditius et al., 2014; Keith et al., 2016b; Keith et al., 2018a). Beyond this economic aspect, pyrite is known as a mineral that forms under a wide range of fluid temperatures, oxidation states and pH conditions (Reed and Palandri, 2006). Several studies have stressed that pyrite chemistry reflects the composition of ore-forming fluids due to its sensitivity to changes in physicochemical fluid composition (Pals et al., 2003; Reich et al., 2013; Deditius et al., 2014; Gregory et al., 2015; Keith et al., 2016a, 2016b; Tardani et al., 2017; Keith et al., 2018a; Gregory et al., 2019). For these reasons, pyrite is ideally suitable for *in situ* analytical studies to decipher the complex and poorly constrained Au and Te ore-forming processes in alkaline-hosted epithermal environments like Cripple Creek. Our results indicate that the combined use of mineralogical and chemical techniques help to define key ore-forming processes and provide important insights into the metal plumbing system of the Cripple Creek epithermal deposit.

2 Geological overview and sample localities

The Cripple Creek Au-Te deposit is located in the southern Rocky Mountains in central Colorado. The world-class low-sulfidation epithermal district (>26.3 Moz Au production, in 2018) is hosted by Oligocene silica-undersaturated alkaline igneous rocks ranging in composition from ultramafic lamprophyres to felsic phonolites suggesting a complex magmatic history of the district (Fig. 1) (Kelley et al., 1998; Jensen and Barton, 2000; Jensen, 2003). The alkaline volcanic complex of Cripple Creek has an elliptical shape, covers an area of about 18 km^2 and is hosted by Precambrian basement rocks. The basement includes a series of granite batholiths (1.65, 1.45 and 1.05-1.1 Ga), as well as subordinate metasediments and metavolcanics (1.7 Ga; Kelley et al., 1998; Kelley and Ludington, 2002; Jensen, 2003).

Magmatic activity at the Cripple Creek complex started at about 33 Ma in a transitional stress regime between Laramide orogeny compression (70 to 42 Ma, Coney, 1976, 1978) and the onset of Rio Grande rift extension (30 Ma, Cappa, 1998) in response to slab rollback (Kelley et al., 1998; Kelley and Ludington, 2002; Jensen, 2003; Jensen and Barton, 2007; Chapin, 2012; Kelley and Spry, 2016). The alkaline melts formed during post-subduction melting of previously metasomatized mantle generating alkali- and volatile-rich oxidized melts and Au-rich magmatic-hydrothermal fluids (Kelley et al., 1998; Kelley and Ludington, 2002; Holwell et al., 2019). Volcanic diatremal breccias (32.5 to 28.4 Ma; Kelley et al., 1998) represent the most widespread lithology in the Cripple Creek alkaline complex (Fig. 1), which formed due to volcanic activity possibly related to phreatomagmatic eruptions in a maar-like environment (Thompson et al., 1985; Jensen, 2003; Jensen and Barton, 2007). The breccia has a phonolitic bulk composition but clasts show a wide compositional range including phonolites, syenites, mafic alkaline rocks and Precambrian rock fragments in variable proportions (Jensen and Barton, 2007).

Later magmatic activity post-dating the breccia formation is documented by a series of intrusions including phonolites, tephriphonolites, phonotephrites, tephrites and ultramafic lamprophyres (Jensen and Barton, 2007; Jensen, 2003). The occurrence of late mafic to ultramafic rock types (e.g., lamprophyres) post-dating the felsic phonolite emplacement suggest a multi-stage magmatic system with magma replenishment, which probably was important for the evolution of the magmatic-hydrothermal system at Cripple Creek (Kelley et al., 1998).

The magmatic system was accompanied by multi-stage hydrothermal activity, which started with the emplacement of the earliest igneous rocks (~32.5 Ma) and continued beyond the latest magmatic stage, represented by the lamprophyres (~28.4 Ma) that pre-date the main stage of Au formation (Kelley et al., 1998; Jensen, 2003; Rampe et al., 2005). Two main styles

of mineralization can be distinguished at Cripple Creek: (1) low-grade Au ores with disseminated pyrite of widespread occurrence in permeable brecciated rocks and (2) high-grade Au-telluride veins (Kelley et al., 1998). Samples presented in this study were recovered from three localities in the Cripple Creek diatreme: the actively operated open pits of (1) WHEX, (2) Cresson (Ruby stockpile) and (3) the historic mine site of Vindicator Valley (Fig. 1). The sample set includes low-grade disseminated and high-grade vein-type ores (electronic supplement, Table A1) providing information on the ore-forming processes and their effect on the Te distribution in all major ore-types of Cripple Creek.

3 Methods

3.1 Bulk ore chemistry

A total of 17 bulk ore samples including low-grade disseminated ore and high-grade vein material were crushed and milled to a homogenous powder (electronic supplement, Table A1). Pressed powder pellets were produced from mixing 7 g of sample powder with 12 to 15 drops of a PVA solution (Moviol 8-88). The minor and trace element composition (electronic supplement, Table A2) of the pressed powder pellets (including duplicates) were determined at the University of Leicester on a PANalytical Axios-Advanced XRF spectrometer using a PANalytical SuperQ system with IQ+, WROXI and ProTrace extensions, as the controlling and processing software. The XRF analysis was calibrated by international reference materials (electronic supplement, Fig. A1); quantitative concentrations were calculated by regressing the count rates of the unknown material against international standards of certified composition (Govindaraju, 1994; Imai et al., 1995, 1996, 1999).

Bulk ore samples with Te concentrations near or below the limit of detection (0.6 ppm Te) of XRF spectrometry were analyzed at Cardiff University and ALS Laboratories (method ME-MS41) by ICP-MS using aqua regia digest (n=13) (electronic supplement, Table A3). The

aqua regia digest used sample weights accurately weighed close to 0.5 g of milled and dried powder. The sample material was digested in 5 ml of concentrated aqua regia (3 parts HCl:1 part HNO_3) inside a sealed 15 ml capacity screw-top Teflon vial on a hotplate at ~150°C for 16-18 hours. Samples were allowed to cool and settle before 0.5 ml of digest solution was extracted using a pipette and diluted to 5 ml with 18.2 mW (milli-Q) deionized water. Diluted samples were analyzed on a Thermo X Series 2 ICP-MS. Highly chalcophile elements, such as those that are associated with sulfide minerals are assumed to be close to 100% extracted by aqua regia. Tellurium concentrations analyzed by XRF and ICP-MS using aqua regia digest are identical confirming the high quality of the Te data presented here (e.g., 3.87 vs. 3.74 ppm, CC-16-02.2; 0.57 vs. 0.61 ppm; VV-16-03.3). Additionally, Au was analyzed in these samples by fire assay at ALS Laboratories (electronic supplement, Table A3). Lower limits of detection, blanks and analyses of reference materials are listed in the electronic supplement (electronic supplement, Table A4).

Gold was analyzed by a number of methods (XRF, Leicester; aqua regia, Cardiff; fire assay, ALS) due to the capabilities of the different analytical techniques. X-ray fluorescence is particularly good in analyzing samples with higher Au contents (>30 ppm), while at lower concentrations (<30 ppm) fire assay and aqua regia digest are the preferred techniques. Therefore, we defined a 30 ppm threshold for the Au data using XRF at higher (>30 ppm) and a combination of aqua regia and fire assay data at lower concentrations (<30 ppm).

3.2 Micro-analytical techniques

Prior to the geochemical analysis, 20 polished thick sections and 2 polished thin sections of low-grade disseminated and high-grade vein-type ore from the three sampling sites were petrographically examined to identify the different mineral phases (electronic supplement, Table A1). Unknown minerals were identified and major element mapping was performed by a JEOL JXA-8600 Superprobe at the University of Leicester using energy-

197 dispersive x-ray spectrometry (EDS). Wavelength-dispersive x-ray spectrometry (WDS,
198 n=285) was used together with EDS (n=562) for the major element analysis of the different
199 sulfide, sulfosalt and telluride phases (n=847, electronic supplement, Table A5). The
200 quantitative analyses were carried out with a focused beam at an acceleration voltage of 20 kV
201 and a beam current of 20 nA. Count times for WDS analyses were set to 20 and 10 s for the
202 peak and background measurements, respectively. The WDS was calibrated by the following
203 reference materials: FeS_2 (Fe, S), Cu (Cu), Zn (Zn), InAs (As), PbTe (Pb). Energy-dispersive
204 x-ray spectrometry has been normalized to 100 wt. % (Table A5). Stoichiometric calculations
205 of the cation sums were used for data quality assurance. Most analyses displayed an error ≤3
206 at. % with respect to the ideal stoichiometric composition of pyrite. Each spot analyzed by
207 electron microprobe was marked on a back-scattered electron image for the subsequent analysis
208 of the same mineral grain by LA-ICP-MS (n=426). The S contents determined by electron
209 microprobe analysis were used for the internal standardization of the LA-ICP-MS analyses
210 (electronic supplement, Table A6).
211 Laser ablation ICP-MS (electronic supplement, Table A1) was carried out at the
212 University of Leicester using a New Wave Research-ESI 213 nm laser unit attached to a
213 ThermoScientific ICAP-Q quadrupole ICP-MS. Helium was used as carrier gas with a mass
214 flow rate of 650 ml/min. A single spot ablation pattern with a frequency of 10 or 20 Hz, an
215 irradiance of 0.77 GW/cm^2 and a fluence of 4 J/cm^2 was used. A beam diameter of 25 µm was
216 applied and on occasion of 20 µm according to pyrite crystal size. In this respect, pyrite from
217 high-grade material could only rarely be analysed due to grain sizes <<20 µm (n=27, Table 1).
218 Analyses of areas where inclusions were large enough to be visible by (electron) microscopic
219 techniques were avoided. Total run time was set to 65 to 70 s including 20 to 25 s of pre-
220 ablation blank analysis. The UQAC FeS-1 reference material
221 (https://sulfideslasericpms.wordpress.com); a homogeneous natural sulfide nano-powder

doped with a range of trace elements for matrix-matched calibration of Fe-sulfides by LA-ICP-MS was used for external standardization. Analytical precision and accuracy were monitored by the repeated analysis of FeS-1 and MASS-1 (USGS). Relative standard deviations (RSD) were <10% for all analyzed elements (Table A7). To monitor the instrument drift, sulfide standards were analyzed several times a day. Quantitative spot analysis was combined with qualitative LA-ICP-MS mapping to display potential patterns of trace element zoning in single pyrite crystals. A beam diameter of 5 µm and a scan speed of 3 µm/s was used for the mapping; all other operating conditions were identical to the spot analysis. Trace element concentrations, minimum detection limits (electronic supplement, Table A6) and maps were processed by the Iolite software package developed at the University of Melbourne (https://iolite-software.com).

Mineral and bulk ore data are rarely normally distributed, and therefore the geometric mean and geometric standard deviation (GSD) is used for the data presentation (Table 1, Fig. 2) (Reimann and Filzmoser, 2000; Gregory et al., 2015; Gregory et al., 2019).

4 Results

4.1 Bulk ore chemistry

Bulk ore data show a significant enrichment in Au and Te reaching up to 1694 and 2235 ppm, respectively (Table 1), in the high-grade vein-type compared to the low-grade host rock ore (Table 1, Fig. 2). Tellurium and Au are also significantly enriched in the high-grade ore compared to any of the analyzed sulfide phases (Fig. 2). There is a general depletion in most trace elements, except Co, Ni and Zn, in the low-grade host rock compared to the high-grade vein-type ore (Fig. 2). Arsenic concentrations between the low- and high-grade ore are indistinguishable, which may be due to incomplete separation of the high-grade veins from the low-grade host rocks prior to bulk ore analysis (Fig. 2).

4.2 Sulfide and sulfosalt petrography

The petrographic observations reveal that pyrite represents the most abundant ore phase at Cripple Creek occurring in both, the low-grade host rock and high-grade vein-type ores (Fig. 3). This includes tiny (< 5 μm), but locally abundant, sub- to euhedral pyrite crystals in breccia fragments (py 1, Fig. 4A), larger anhedral and dissolved pyrite (py 2) associated with pyrite of large euhedral appearance (py 3) typically occurring between the breccia fragments (Fig. 4A and B), as well as larger subhedral to euhedral pyrite (py 4) and tiny pyrite crystals of accessory and euhedral appearance (py 5) hosted in the high-grade vein-type ores (Fig. 5A). Therefore, five different types of pyrite mineralization (py1 to py5) can be distinguished in the low-grade disseminated host rock and high-grade vein-type ores (Fig. 3).

All other sulfide phases typically occur in trace amounts over the entire sample set with occasionally higher abundances in individual samples (Fig. 3). Galena and sphalerite often show a close association with pyrite either as individual phases surrounding py 3 (Fig. 4 C and D) or as inclusions and along cracks in py 3 (Fig. 5B and C). Similarly, chalcopyrite (Fig. 5C) and pyrrhotite (Fig. 4E) occur in trace amounts usually as inclusions in py 3. Sulfosalts were rarely observed at Cripple Creek (Fig. 3); they include tennantite occurring as inclusions in sphalerite (Fig. 4D) and another unidentified Pb-Sb(-As) sulfosalt identified by EDS.

4.3 Telluride and precious metal mineralogy and chemistry

Electron microscopy and EDS were used for the identification and classification of the different telluride phases. Optical microscopy provided only limited information due to the small size of the telluride crystals. In total, five different telluride phases were identified: calaverite ($AuTe_2$), coloradoite (HgTe), petzite (Ag_3AuTe_2), hessite (Ag_2Te) and altaite (PbTe) (Fig. 3). Silver-rich tellurides show a close association with native Ag, whereas Au-tellurides are commonly accompanied by native Au (4.91 to 13.2 wt. % Ag, 86.8 to 95.1 wt.% Au).

Energy dispersive spectrometry revealed that the analyzed telluride phases usually show a near stoichiometric composition (electronic supplement, Fig. A2, Table A5).

Silver-rich tellurides, i.e. hessite and petzite, and native Ag usually occur as accessory phases in the low-grade disseminated host rock ores typically as inclusions in py 3 (Fig. 3 and 5B). In contrast, all other telluride phases are usually hosted in the high-grade vein-type ore together with abundant quartz and fluorite gangue (Fig. 3, 6 and 7). Calaverite is by far the most abundant telluride phase in the Cripple Creek ores showing a close relationship with py 4 (Fig. 5A) and other tellurides, such as petzite (Fig. 5D). Mapping by EDS revealed that tellurides in the high-grade vein-type ores usually occur in clusters or aggregates composed of different tellurides and native Au. For example, altaite and coloradoite commonly surround calaverite, while native Au is attached to coloradoite (Fig. 6 and 7).

4.4 Sulfide major and trace element chemistry

Pyrite, the most abundant sulfide phase at Cripple Creek (Fig. 3), shows a distinct variation in its As contents ranging from trace element levels in stoichiometric pyrite to major element concentrations in As-rich (arsenian) pyrite reaching 3.4 wt. % or 1.9 at. % (Table 1). Arsenic in pyrite shows a negative correlation with S; no systematic relationship has been observed with Fe (Fig. 8).

Sulfides analyzed for their trace element composition are enriched in the analyzed transition (e.g., Co, Cu, Zn, Pb), semi (e.g., Se, As, Te) and precious (e.g., Au and Ag) metals compared to bulk continental crust (Fig. 2) (Wedepohl, 1995). Chalcopyrite, sphalerite and galena are the main hosts for Cu, Zn and Pb, respectively. However, trace element concentrations vary significantly between the different sulfide phases (Fig. 2). Pyrite, for example, represents the main host for Co, Ni, As, Mo, Te and Au. In contrast, sphalerite shows high concentrations in Cd but is depleted in all other trace elements compared to pyrite. Galena is also known to incorporate trace elements in high concentrations (George et al., 2015). At

294 Cripple Creek, galena shows a distinct enrichment in Se, Ag, Sb, Tl and Bi compared to the
295 other sulfides analyzed in this study (Fig. 2). Chalcopyrite could not be analyzed by LA-ICP-
296 MS for its trace element composition due to its small grain size (Fig. 5C).

297 Laser ablation ICP-MS mapping was conducted to study the distribution of trace
298 elements on the mineral scale (Fig. 9). Complex zoning patterns were observed in py 3 (low-
299 grade ore) from Vindicator Valley and Ruby. Gold and As, for example, are enriched at the
300 rims of the pyrite crystal at Vindicator Valley, while at Ruby a clear concentric/growth zoning
301 with sharp boundaries was observed. Similarly, Co and Ni are strongly enriched in py 3 from
302 Ruby compared to Vindicator Valley, also showing a distinct concentric zoning (Fig. 9).
303 Interestingly, Au-As and Co-Ni-rich zones in py 3 from Ruby alternate (cf. Tardani et al., 2017;
304 Román et al., 2019). Tellurium is enriched at Vindicator Valley with a bimodal distribution
305 displayed by an enrichment in the core and along the py 3 rim. Silver is enriched at Ruby
306 compared to Vindicator Valley but without any systematic pattern in the pyrite crystal.

307 Bivariate diagrams between As-Au and As-Te show a positive correlation (Fig. 10).
308 Pearson correlation coefficients (linear R values) are listed in the electronic supplementary
309 material (Table A8), which includes all bivariate combinations for the trace elements analyzed
310 in pyrite.

311 **5 Discussion**

312 *5.1 Paragenetic sequence of ore-formation*

313 A total of seven different stages of ore formation can be distinguished at Cripple Creek
314 (Fig. 3) (Dye, 2015). Five distinct generations of pyrite mineralization from early py 1 to late
315 py 5 were identified. This includes py1 to py 3 in the low-grade disseminated host rock ore
316 (Fig. 4A and B), as well as py 4 and py 5 in the later high-grade quartz-fluorite veins (Fig. 5A)
317 that cut the mineralized Cripple Creek breccia body, i.e. the low-grade host rock ore. Textural

differences between anhedral and porous py 2 and euhedral py 3 were interpreted to be due to a dissolution event separating the two pyrite generations (Fig. 3, 4A and B) (Dye, 2015). Pyrite formation during the main base metal sulfide (BMS) stage is accompanied by pyrrhotite, sphalerite, galena and chalcopyrite (Fig. 3). Two principal formation conditions are suggested for these sulfide phases: (1) deposition prior to py 2/3 due to an inclusion-related appearance and (2) precipitation subsequently to py 2/3 indicated by an occurrence in the pore space (Fig. 5B), along intra-crystalline cracks (Fig. 5C) or as a later phase surrounding pyrite 2/3 (Fig. 4C and D). Tennantite inclusions in sphalerite that surrounds py 2/3 (Fig. 4D) suggest a formation before or together with late sphalerite during the BMS stage (Fig. 3). Molybdenite has been used an indicator for a potential deeper porphyry ore body beneath the Cripple Creek epithermal system (Jensen and Barton, 2007; Kelley and Spry, 2016). Rare earth elements seem to be primarily hosted by monazite in the main BMS ores (Fig. 3), where rutile occurs at the transition to the high-grade mineralization possibly replacing py 3 (Fig. 4F).

The early Ag(-Au) tellurides pre-date the main BMS stage (Fig. 3 and 5B), whilst the high-grade Au(-Ag) telluride formation is hosted by late quartz-fluorite veins (Fig. 3). Calaverite represents the first telluride phase precipitating in the high-grade vein-type ore (Fig. 6 and 7), which post-dates the vein-hosted py 4 generation (Fig. 5A). Petzite (Fig. 5D) and coloradoite (Fig. 7) follow calaverite together with altaite (Fig. 6) and native Au (Fig. 7) that form late during the Au(-Ag) telluride high-grade stage (Fig. 3).

The high-grade vein-host rock contact characteristically has a quartz seam free of fluorite or with only minor amounts suggesting a slightly earlier onset of quartz formation compared to fluorite (Fig. 3). The occurrence of tellurides in the center of the high-grade veins along with fluorite (Fig. 7B) also indicate that quartz started to crystallize prior to the main Au-Te stage (cf. Kelley et al., 1998; Dye, 2015). In summary, Cripple Creek shows a typical sequence of ore-formation for alkaline igneous rock-hosted epithermal deposits, as indicated

by the early low-grade main BMS mineralization followed by high-grade Au(-Ag) telluride precipitation (Cooke and McPhail, 2001; Kelley and Ludington, 2002). These mineralogical differences suggest significant changes in the fluid conditions during ore-formation (cf. Section 5.3 and 5.4).

5.2 Trace element incorporation and speciation

Pyrite can incorporate a wide range of trace elements in significant amounts either as lattice bound substitutions for Fe and S or as micro- to nano-sized inclusions (Pals et al., 2003; Reich et al., 2005, 2013; Deditius et al., 2014; Gregory et al., 2014, 2015; Keith et al., 2016a, b; Deditius and Reich, 2016; Keith et al., 2018a; Martin et al., 2019; Pokrovski et al., 2019). Arsenic is a common constituent in the pyrite lattice substituting for tetrahedrally-coordinated S^- or octahedrally-coordinated Fe^{2+} as As^- or $As^{2+/3+}$, respectively (Fleet and Mumin, 1997; Savage et al., 2000; Deditius et al., 2008; Keith et al., 2018a). Hence, the negative correlation of As and S in pyrite from Cripple Creek (Fig. 8) strongly suggests a substitution of anionic As for S^- in the tetrahedral site. The different covalent radii of As (119 pm) and S (105 pm), as well as the higher amounts of As in arsenian pyrite cause an expansion of the unit cell. This substitution also results in significant lattice defects, vacancies and Fe deficiencies in arsenian pyrite facilitating the incorporation of heavier and larger elements, such as Au (136 pm) and Te (138 pm) (Fleet and Mumin, 1997; Reich et al., 2005; Keith et al., 2018a; Pokrovski et al., 2019). Chouinard et al. (2005) proposed that the association of Te and As is controlled by the crystal-chemical properties of pyrite, which is reflected by sector zoning in pyrite crystals with the preferential incorporation of these elements on the (110) surface in the cubic crystal system. In contrast, concentric/growth zoning as observed in pyrite from Cripple Creek (Fig. 9) forms under non-equilibrium conditions with little or no structural control (Deditius et al., 2009; Tardani et al., 2017; Román et al., 2019), which implies that the trace element composition of pyrite from Cripple Creek is diagnostic for fluid-related processes.

High concentrations of trace elements, such as Au and Te, in LA-ICP-MS data can be due to the incorporation into the lattice of a host mineral, or by trapping of mineralogically distinct inclusions within a larger mineral. For instance, spikes of Pb, Ag, Au and Te in the time-resolved LA-ICP-MS spectra likely indicate that galena, native Au, Au-telluride (e.g., calaverite) and possibly native Te inclusions are present in pyrite from Cripple Creek (Fig. 11) (Reich et al., 2013; Keith et al., 2016a; Tardani et al., 2017; Román et al., 2019). Empirically derived element solubility limits as a function of As in pyrite (gray dashed lines, Fig. 10) also allow to infer the presence of inclusions or the incorporation of trace elements in solid solution (Reich et al., 2005; Deditius and Reich, 2016; Keith et al., 2018a). The well-established Au solubility line by Reich et al. (2005) highlights that Au commonly occurs in solid solution in pyrite from Cripple Creek (concentrations below the solubility limit). Only a few pyrite (py 4) analyses from Ruby reach Au concentrations above the solubility limit (Fig. 10A) and LA-ICP-MS spectra confirm the presence of native Au inclusions (Fig. 11A). Pyrite that hosts Au-telluride inclusions (Fig. 11B) also plots above the Te solubility limit (Fig. 10B).

In contrast, smooth LA-ICP-MS spectra of pyrite (Fig. 11A, C, E) infer structurally bound elements incorporated by lattice substitution (Gregory et al., 2014, 2015; Keith et al., 2016a; Martin et al., 2019; Román et al., 2019). In this context it is controversial, why some Te analyses with concentrations above the solubility limit (Fig. 10B) display smooth LA-ICP-MS patterns (Fig. 11C, E). This may either be due to (1) the limitation of laser ablation to identify inclusions on the nano-scale, since the spot size is sufficiently larger than the included nano-phase, which are therefore no longer apparent as a spike in time-resolved data, or (2) that the Te solubility line (Fig. 10B) needs to be adjusted (work in progress).

Most pyrite analyses that are characterized by high Te/As ratios (white symbols, above solubility line in Fig. 10B) show Te/Au ratios significantly higher than those of typical Au-tellurides implying that Au-telluride inclusions are likely of minor importance for the Au-Te

393 distribution in pyrite from Cripple Creek (Fig. 12A). Further evidence is given by the
394 decoupled appearance of Au and Te in the core of py 3 from Vindicator Valley and Ruby (Fig.
395 9). This can also be seen in the Au-As and Te-As system (Fig. 10), where the analyzed spots
396 in the mapped area of py 3 from Vindicator Valley (red circles) are enriched in Te (high Te/As)
397 but depleted in Au (low Au/As). Tellurium commonly shows no or only weak correlations with
398 most other trace elements except As, as illustrated in the laser ablation maps (py 3 cores, Fig.
399 9) and the bivariate systems (see Pearson correlation coefficients in the electronic supplement,
400 Table A8). Hence, their seems to be only a limited effect of other trace elements (except As)
401 on the incorporation of Te in pyrite leading to Te solid solution by S substitution (Huston et
402 al., 1995; Chouinard et al., 2005; Kesler et al., 2007; Maslennikov et al., 2009) or possibly
403 native Te inclusions (Fig. 11D). Native Te has also been identified in other alkaline-hosted
404 low-sulfidation epithermal systems, such as Emperor (Fiji; Pals and Spry, 2003) and Boulder
405 County (Colorado; Kelley and Spry, 2016).
406 Silver and Au display a moderate positive correlation in pyrite (R^2=0.49), which may
407 be related to native Au (electrum) inclusions as suggested for Ruby (Fig. 10A and 11A). Some
408 Te-rich pyrites (high Te/As , white symbols) show Te/Ag ratios similar to hessite and other
409 Ag-rich tellurides (Fig. 12B), which may be due to hessite inclusions associated with native
410 Ag in low-grade ore pyrite (Fig. 5B). High concentrations of Ag (up to 880 ppm) were also
411 observed in galena together with Bi (up to 1690 ppm), and hence galena inclusions in pyrite
412 may represent another important Ag host (Fig. 5C and 11E). This is supported by Te/Pb ratios
413 in pyrite lower than typical Pb-telluride phases also suggesting galena inclusions (Fig. 12C).
414 In contrast, pyrite with Te/Pb ratios comparable to Pb-tellurides may indicate inclusions of
415 minerals like altaide (Fig. 6 and 12C). Bismuth-tellurides were not observed petrographically
416 in this or in previous studies indicating that tellurides are an unlikely host for Bi at Cripple
417 Creek. However, Te/Bi ratios of some pyrites are similar to common Bi-tellurides (Fig. 12D)

418 indicating that a local occurrence in pyrite cannot be excluded. Tellurium-trace element ratios
419 higher than those of many common telluride phases (Fig. 12) therefore either imply (1) a Te
420 substitution decoupled from most other trace elements or (2) the occurrence of native Te
421 inclusions (Fig. 11D). This decoupling provides evidence that the ore-forming processes of Te
422 may be distinct compared to those of many other trace metals and metalloids.

423 Cobalt and Ni are typically hosted in pyrite in solid solution by substituting Fe; Co^{2+} →
424 Fe^{2+} and Ni^{2+} → Fe^{2+} (Huston et al., 1995; Maslennikov et al., 2009). It is likely that most of
425 the structurally bound Cu replaces Fe in octahedral sites, which may be due to distortion of the
426 pyrite lattice by the presence of other elements such as As, Sb or Co (Tardani et al., 2017). The
427 coupling and decoupling of trace elements accompanied by the observed concentric/growth
428 zoning in pyrite strongly suggest that ore-formation at Cripple Creek was controlled by
429 complex multi-stage magmatic-hydrothermal processes (cf. sections 5.3 and 5.4) (Jensen,
430 2003; Jensen and Barton, 2007; Dye, 2015).

431 *5.3 Au-Te in pyrite: Tracers for fluid boiling and vapor condensation*

432 Previous studies showed that fluid boiling and conductive cooling along the boiling
433 curve are important, if not primary processes for the deposition of metals and metalloids such
434 as Au and Te in many low-sulfidation epithermal systems (Thompson et al., 1985; Ahmad et
435 al., 1987; Cooke and McPhail, 2001; Simmons et al., 2005; Jensen and Barton, 2007). In
436 addition to trace metal fractionation between the vapor and liquid phase, boiling also leads to
437 a fO_2 and pH increase in the ore-forming fluids due to S^{2-} and H^+ loss into the vapor phase
438 (Drummond and Ohmoto, 1985; Cooke and McPhail, 2001).

439 Trace elements in pyrite are not homogeneously distributed as highlighted by
440 concentric/growth zoning (Fig. 9). The different zones show sharp boundaries suggesting
441 abrupt physicochemical changes in the hydrothermal fluids (e.g., temperature, pH, fO_2, ligand
442 availability, chemical composition) affecting the trace metal solubility and leading to a

443 selective incorporation of trace metals into pyrite (Deditius et al., 2009; Tardani et al., 2017;
444 Román et al., 2019). Continuous processes, such as conductive cooling, would rather result in
445 a gradual/diffused zoning pattern; hence, conductive cooling alone cannot explain the trace
446 metal distribution at Cripple Creek. Therefore, we hypothesize that boiling is an essential ore-
447 forming process for the Au-Te mineralization at Cripple Creek (Fig. 13) (cf. Jensen, 2003).

448 Boiling is an efficient process to precipitate Au from epithermal fluids due to the
449 preferential partitioning of H_2S into the vapor phase, which destabilizes the Au-bisulfide
450 complexes ($Au(HS)_2^-$) in the liquid phase causing Au deposition (Fig. 13) (Cooke and McPhail,
451 2001; Jensen, 2003; Simmons et al., 2005; Keith et al., 2018a). In contrast, at neutral to alkaline
452 pH (7 to 8), moderately reduced conditions (-25 to -35 log fO_2) and temperatures between 200
453 and 300°C, typical for alkaline-hosted low-sulfidation epithermal systems like Cripple Creek
454 (Smith et al., 2017), Te shows a strong affinity to the vapor phase, most likely as $TeO(OH)_2$ or
455 $Te(OH)_4$, with a vapor/liquid distribution coefficient of about 10^4 (Fig. 13) (McPhail, 1995;
456 Cooke and McPhail, 2001; Wallier et al., 2006; Pudack et al., 2009; Grundler et al., 2013).
457 Importantly, native Te associated with py 3 at Cripple Creek (Fig. 11D) is stable at near neutral
458 pH and -25 to -35 log fO_2 (McPhail, 1995; Brugger et al., 2016). This allows the definition of
459 the fluid conditions at the onset of py 3 deposition in the low-grade ores and confirms that
460 under these conditions Te can strongly partition into the vapor phase during boiling, while Au
461 is concentrated in the liquid phase (Fig. 13). This leads to the characteristic decoupling of Au
462 and Te during the early stages of py 3 growth between Vindicator Valley and Ruby (Fig. 9 and
463 13).

464 We propose that this Au-Te fractionation pattern can be explained by a combination of
465 fluid boiling and aqueous vapor condensation. Boiling of hydrothermal fluids would lead to
466 the precipitation of Au and the loss of Te to an exsolving aqueous vapor phase, which is
467 illustrated by the Au enrichment and Te depletion in the core of py 3 from Ruby (Fig. 9G, H

468 and 13). In natural systems boiling most likely occurs in an open system representing the most
469 efficient process for metal fractionation and deposition. Open system boiling can be described
470 by Rayleigh fractionation processes, i.e. every vapor increment is removed from the boiling
471 liquid (Drummond and Ohmoto, 1985), which results in the spatial separation of elements with
472 an affinity to either the liquid or vapor phase, such as Au and Te, respectively. The subsequent
473 condensation of the Au-poor and Te-rich vapors into low temperature metal-bearing meteoric
474 waters, possibly at shallower crustal levels, and the interaction of these evolved fluids with the
475 adjacent wall rocks results in an fO_2 decrease in the ore-forming fluids due to host rock Fe^{2+}
476 oxidation causing Te precipitation (Fig. 13) (Jensen and Barton, 2007; Grundler et al., 2013;
477 Gao et al., 2017; Keith et al., 2018a), which can therefore explain the high Te and low Au
478 contents in py 3 cores from Vindicator Valley (Fig. 9A and B). This is supported by $\delta^{34}S$ values
479 of -5.6 and -0.1 ‰ in creedite ($Ca_3Al_2(SO_4)(F,OH)_{10}•2(H_2O)$), a hydrothermal sulphate phase
480 in the Cripple Creek deposit, which were interpreted to be the result of H_2S gas condensation
481 in a steam heated near surface environment (Jensen, 2003). A similar process for the deposition
482 and spatial separation of Au and Te has been applied to the low-sulfidation epithermal Au-Ag-
483 Te mineralization at Acupan, Philippines (Cooke and McPhail, 2001).

484 Interestingly, Au-As and Ni-Co rich zones are decoupled in py 3 from Ruby suggesting
485 a slightly earlier precipitation of the latter (Fig. 9). Boiling causes pyrite precipitation but only
486 during the initial stages before significant H_2S loss (Drummond and Ohmoto, 1985). At the
487 onset of boiling pH increases sharply during the first increments of H_2-rich vapor release
488 (Drummond and Ohmoto, 1985). This significantly affects the stability of base metals in
489 solution, such as Fe, Co and Ni likely leading to their contemporaneous precipitation and
490 incorporation in pyrite (Seyfried and Ding, 1995; Seyfried et al., 1999; Liu et al., 2011). In
491 contrast, higher pH conditions will increase the solubility of the Au-bisulfide complex
492 ($Au(HS)_2$) until H_2S starts to exsolve into the vapor during continuous boiling (Drummond and

493 Ohmoto, 1985). Similar to Au, it is suggested that As also precipitates from the liquid phase as
494 indicated by their close association in py 3 (Fig. 9G and J) (Pokrovski et al., 2013). This is in
495 good agreement with the recent results of Tardani et al. (2017) and Román et al. (2019) arguing
496 that the alternation of Co-Ni- and Au-As-rich zones is a typical boiling texture in pyrite due to
497 fluctuations between gentle and vigorous boiling, respectively. These variations in fluid boiling
498 must be due to changes in pressure, temperature or fluid salinity.

499 The enrichment of Au and Te along py 3 rims indicates that Au-Te fractionation ceased
500 or became inefficient with continued py 3 formation (Fig. 9 and 13). Grundler et al. (2013)
501 emphasized that the affinity of Te to the vapor phase during fluid boiling strongly decreases
502 under more oxidized conditions (above -25 to -30 log fO_2) at pH 7 to 8, which is suggested for
503 the Au-Te-rich fluids forming the high-grade ores at Cripple Creek (Smith et al., 2017). Small
504 amounts of Te would still partition into the vapor phase under these conditions but most Te
505 would concentrate in the liquid phase together with Au leading to the coupled enrichment of
506 Au and Te along the py 3 rims at Ruby (Fig. 9G and H). However, this cannot explain the
507 combined Au-Te enrichment in the vapor-dominated Vindicator Valley ores (Fig. 9A and B).
508 Therefore, we propose that an increased magmatic volatile influx to the Cripple Creek
509 hydrothermal system during the transition from the low-grade main BMS stage (late stage of
510 py 3, Fig. 3) and the high-grade vein-type ore is responsible for the Au-Te enrichment along
511 the py 3 rims (Fig. 9 and 13; cf. Section 5.3).

512 *5.4 Constraints on the source of Au and Te*

513 Fluids of magmatic origin are considered to be a common and important source of
514 metals, such as Au and Te, in alkaline-hosted epithermal systems (Fig. 13) (Cooke and
515 McPhail, 2001; Zajacz et al., 2010; Smith et al., 2017). Several lines of evidence suggest a
516 contribution of magmatic volatiles to the Cripple Creek hydrothermal system including (1)
517 stable isotopes, (2) mineral stabilities and (3) trace metal chemistry.

518 *(1) Stable isotopes:* Hydrothermal sulfides from Cripple Creek that are associated with
519 the Au-Te mineralization are characterized by low $\delta^{34}S$ values ranging from -18.6 to +2.9 ‰
520 with most analyses showing <0 ‰, which are interpreted to be the result of the
521 disproportionation of magmatically derived SO_2 to ^{34}S enriched H_2SO_4 and ^{34}S depleted H_2S
522 contributed to the epithermal system (Jensen, 2003; Jensen and Barton, 2007; Kelley and Spry,
523 2016). Similarly, $\delta^{18}O$ values between +2 and +9 ‰ in quartz from the high-grade vein-type
524 ores are consistent with a magmatic fluid origin and variable proportions of meteoric water
525 (Jensen, 2003; Jensen and Barton, 2007; Kelley and Spry, 2016).
526 *(2) Mineral stabilities:* The occurrence of tennantite (Fig. 4D) towards the end of the
527 main BMS stage (Fig. 3) indicates a shift from low- to intermediate sulfidation conditions
528 (Sensu stricto, Einaudi et al., 2005) possibly due to an increasing contribution of oxidized
529 magmatic fluids during the transition from the meteoric water-dominated low-grade BMS to
530 the more magmatically controlled high-grade vein-type Au-Te mineralization.
531 *(3) Trace element chemistry:* The increasing contribution of magmatic fluids is also
532 supported by the trace element distribution in pyrite showing an outer enriched zone in volatile
533 elements including As, Te and Au (Fig. 9), as well as Sb, Cu and Bi (not shown) that are
534 considered to be of magmatic volatile origin (Cooke and McPhail, 2001; Pokrovski et al., 2002;
535 Williams-Jones and Heinrich, 2005; Pokrovski et al., 2008, 2013; Wohlgemuth-Ueberwasser
536 et al., 2015). Tellurium, for example, may be transported as H_2Te (g) and Te_2 (g) in magmatic
537 volatiles (Cooke and McPhail, 2001). In contrast, the deposition of native Ag, hessite and
538 pyrrhotite (Fig. 4E and 5B) prior or during the earliest stage of the low-grade main BMS
539 mineralization (Fig. 3) indicates low-sulfidation conditions dominated by more reduced
540 meteoric fluids (Barton and Skinner, 1979; Zhang and Spry, 1994; Cook et al., 2009b; Grundler
541 et al., 2013), which also explains the absence of hessite and native Ag in the high-grade Au-Te
542 vein-type ores (Fig. 3).

543 Alternatively, metals can be leached from the host rocks by hydrothermal fluids, which
544 may be particularly important in the formation of the meteoric water-dominated BMS ores.
545 Smith et al. (2017) and Keith et al. (2018a) showed that the Te distribution in low-sulfidation
546 epithermal ores may be controlled by the Te content in the alkaline host rocks from which Te
547 can efficiently be mobilized by neutral to alkaline fluids. Alkaline rocks associated with
548 epithermal mineralization in post-subduction settings are typically enriched in Te due to
549 melting of previously metasomatized mantle during subduction zone magmatism (Jensen and
550 Barton, 2000; Jensen and Barton, 2007; Schirmer et al., 2014; Holwell et al., 2019). At Cripple
551 Creek, late stage mafic and ultramafic igneous rocks follow the more felsic magmatic system.
552 The main Au-Te mineralization occurs in association with the late stage lamprophyre
553 emplacement (Kelley et al., 1998; Jensen and Barton, 2007). Gold and Te represent compatible
554 elements during magma evolution leading to an enrichment in mafic and ultramafic rocks
555 (Patten et al., 2013; Jenner et al., 2017). Hence, it is reasonable to conclude that the ultramafic
556 lamprophyres may represent another source for Au and Te (Rock et al., 1988).
557 The relationship between magmatic fluid release and the onset of sulfide saturation is
558 critical for the behavior of chalcophile metals during magmatic differentiation (Keith et al.,
559 2018b). The sulfide saturation limit strongly depends on the fO_2, i.e. the S^{2-}/SO_4^{2-} ratio of the
560 silicate melt. Hence, sulfide saturation will be reached later during magmatic differentiation in
561 more oxidized melts and the loss of chalcophile metals into immiscible sulfides liquids is
562 minimized (Kelley and Ludington, 2002; Jenner et al., 2010; Keith et al., 2017). Alkaline melts
563 probably reach volatile saturation early during their evolution and due to the suppression of
564 immiscible sulfide liquid segregation it is likely that chalcophile elements with a volatile
565 affinity, such as Au and Te, strongly partition into an exsolving volatile phase (Kelley and
566 Ludington, 2002; Edmonds et al., 2018; Keith et al., 2018b). Later mixing of these metal-
567 bearing more oxidized magmatic volatiles with evolved meteoric water in the shallower

568 epithermal environment results in the formation of Au-Te-rich ore-forming fluids (Fig. 13)
569 (Cooke and McPhail, 2001; Kelley and Ludington, 2002; Ronacher et al., 2004; Dye, 2015).
570 This could likely be a process applicable to Cripple Creek, since tellurides were only identified
571 to about 1000 m depth, emphasizing that external meteoric fluids were involved in their
572 deposition (Jensen, 2003).

573 *5.5 Formation conditions of the high-grade Au-telluride veins*

574 Stable isotope thermometry and fluid inclusion studies provide evidence for decreasing
575 fluid temperatures from the low-grade main BMS stage to the high-grade vein-hosted Au-
576 telluride ores (Fig. 13) (Dwelley, 1984; Thompson et al., 1985; Saunders, 1986; Jensen, 2003;
577 Jensen and Barton, 2007). Sulphur isotope thermometry on galena-pyrite pairs suggest an ore-
578 forming temperature of 223 to 277°C for the low-grade main BMS stage at Cresson (Jensen,
579 2003), one of the sample localities in this study (Fig. 1). Slightly higher temperatures between
580 250 and 350°C were estimated for the pyrite deposition by Thompson (1985) in the Ajax vein
581 system from deeper stratigraphic levels at Cripple Creek. Temperature estimates for the Au-Te
582 ore formation are consistently lower (<200°C) compared to the BMS ores. Fluid inclusion
583 homogenization temperatures in quartz and fluorite hosted in the high-grade Au-telluride veins
584 imply ore-forming temperatures between 105 and 159°C for the Au-Te ores. Similar
585 temperatures (131 to 175 °C) were estimated by Saunders (1986) for the telluride formation at
586 Cresson, whereas Jensen (2003) proposed slightly higher temperatures in the range of 125 to
587 200°C.

588 The lower temperature fluids that precipitated the Au-Te ore were suggested to be of
589 alkaline composition and the occurrence of vapor-rich inclusions implies that boiling was an
590 important process during the formation of the high-grade Au-telluride veins (Fig. 13) (Jensen,
591 2003; Jensen and Barton, 2007). The vein-related occurrence of the Au-tellurides indicates a
592 strong structural control on their mineralization. Hence, it is likely that the ore-forming fluids

593 rose along structural pathways with little conductive cooling until they reached the boiling
594 curve at shallow crustal depth (<1000 m) leading to Au-Te precipitation (Fig. 13) (cf. Cooke
595 and McPhail, 2001). At lower fluid temperatures, boiling processes are stronger and more
596 efficient in precipitating metals contemporaneously, which is due to a less distinct vapor-liquid
597 separation of different volatile species such as H_2, CH_4, CO_2, H_2S, SO_2 (Drummond and
598 Ohmoto, 1985) and possibly associated metals with a vapor and liquid affinity, such as Te and
599 Au, respectively (cf. Section 5.3). At lower fluid temperatures and higher fO_2, caused by the
600 magmatic volatile influx, most of the Te will probably remain in the liquid phase together with
601 Au (Grundler et al., 2013) and the contemporaneous precipitation of these metals results in the
602 formation of calaverite in the high-grade vein-type ores (Fig. 3 and 13). Jensen and Barton
603 (2007) argued that the reaction of the ore-forming fluids with Fe-bearing mafic minerals due
604 to host-rock sulfidation may also trigger the Au deposition. Importantly, recent studies showed
605 that the solubility of Te is highly sensitive to changes in fO_2 and that host rock Fe^{2+} oxidation
606 due to fluid-rock interaction represents an efficient precipitation process for Te (Gao et al.,
607 2017; Keith et al., 2018a). Therefore, it is likely that the suppression of Te partitioning into the
608 vapor phase during boiling combined with fluid-host rock interaction are critical processes for
609 the Au-telluride formation at Cripple Creek.
610 The early deposition of calaverite followed by coloradoite and petzite and the final
611 formation of altaite and native Au in the high-grade vein-type ores (Fig. 3 and 13) reflects
612 compositional changes during fluid evolution. Thermodynamic modelling by Grundler et al.
613 (2013) shows that the stability of different Te and Au phases, such as calaverite and native Au
614 strongly depends on fluid pH and fO_2. The presented paragenetic sequence possibly suggests
615 increasing pH and fO_2, as well as decreasing fTe_2 from early calaverite to late native Au. It is
616 known that fluid boiling causes a pH and fO_2 increase in the liquid phase (Drummond and
617 Ohmoto, 1985), and hence it is likely that the telluride and native Au paragenesis reflects a

618 continuous boiling process at fluid temperatures (105 to 200°C) lower than those of the BMS
619 stage (220 to 350°C). The thermodynamic calculations by Grundler et al. (2013) further imply
620 a change in the Te speciation in the ore-forming fluids from Te^{2-} during telluride precipitation
621 to TeO_3^{2-} at the stage of native Au formation.

622 **6 Summary and conclusions**

623 The combined use of petrographic and microanalytical techniques including
624 quantitative spot analyses and qualitative mapping by LA-ICP-MS provide important
625 information on ore-forming processes and allow to define the incorporation mechanisms of
626 trace elements into various sulfides. Two main ore-types can be distinguished at Cripple Creek:
627 (1) low-grade disseminated pyrite-rich ores of widespread appearance in the permeable
628 brecciated rocks and (2) high-grade Au-telluride veins including calaverite, coloradoite,
629 petzite, altaite and native Au.

630 Pyrite at Cripple Creek hosts Te and Au in solid solution or as native Au, Au-Ag-
631 telluride and possibly native Te inclusions. Laser ablation mapping of pyrite revealed well
632 developed trace element concentric/growth zoning. We propose that these patterns are likely
633 the result of abrupt compositional changes in the ore-forming fluids caused by boiling, which
634 fractionates Te from Co, Ni, As and Au between the vapor and liquid, respectively. Later
635 condensation of the Te-rich vapors in metal-bearing meteoric waters results in the precipitation
636 of Te-rich but Au-poor pyrite as observed at Vindicator Valley.

637 Stable isotopes, mineral stabilities and trace element systematics further suggest that
638 the high Te concentrations in the high-grade vein-type ores are likely due to a magmatic volatile
639 contribution increasing fluid fO_2. Mixing of these magmatically derived fluids with meteoric
640 waters led to a temperature decrease (105 to 200°C) resulting in fluid boiling under lower
641 pressure condition (at crustal depth <1000 m) compared to the BMS stage, where fluid
642 temperatures reached 220 to 350°C. Under these conditions, boiling processes are stronger and

643 volatile species (e.g., H_2, CO_2, H_2S, SO_2) partition into the vapour phase contemporaneously
644 without a selective partitioning over time with proceeding fluid boiling. The more oxidized
645 character of the fluids further suppressed the Te fractionation to the vapor phase finally
646 resulting in the contemporaneous precipitation of Au and Te in the high-grade veins at Cripple
647 Creek.

648 **Acknowledgments**

649 The authors would like to thank the associate editor Z. Zajacz and the reviewers D.
650 Gregory, A. Deditius and an anonymous reviewer for their comments that improved the quality
651 of the manuscript. We thank Newmont Mining Corporation for providing us access to the
652 Cripple Creek deposit and for assistance during the sampling campaign. This study was funded
653 by the UK Natural Environment Research Council (NERC); Minerals Security of Supply (SoS)
654 grant NE/M010848/1, Tellurium and Selenium Cycling and Supply (TeaSe).

655 **References**

656 Ahmad M., Solomon M. and Walshe, J. L. (1987) Mineralogical and geochemical studies of
657 the Emperor gold telluride deposit, Fiji. *Econ. Geol.* **82**, 345–370.

658 Barton P. B. and Skinner B. J. (1979) Sulfide mineral stabilities. In *Geochemistry of*
659 *hydrothermal ore deposits* (ed. H. L. Barnes). John Wiley and Sons, New York, pp. 278–
660 403.

661 Brugger J., Liu W., Etschmann B., Mei Y., Sherman D. M. and Testemale D. (2016) A review
662 of the coordination chemistry of hydrothermal systems, or do coordination changes
663 make ore deposits? *Chem. Geol.* **447**, 219-253.

664 Cappa J. A. (1998) Alkalic igneous rocks of Colorado and their associated ore deposits.
665 *Colorado Geological Survey, Resource Series* **35**, 1–137.

666 Chapin C. E. (2012) Origin of the Colorado Mineral Belt. *Geosphere* **8**, 28–43.

667 Chouinard A., Paquette J. and Williams-Jones A. E. (2005) Crystallographic controls on trace-
668 element incorporation in auriferous pyrite from the Pascua Epithermal high-sulfidation
669 deposit, Chile-Argentina. *Can. Mineral.* **43**, 951–963.
670 Ciobanu C. L., Cook, N. J., and Spry, P. G. (2006) Preface - Special Issue: Telluride and
671 selenide minerals in gold deposits - how and why? *Miner. Petrol.* **87**, 163–169.
672 Coney P. J. (1976) Plate tectonics and the Laramide Orogeny: Tectonics and mineral resources
673 of southwestern North America. *Special Publication of the New Mexico Geological*
674 *Society* **6**, 5–10.
675 Coney P. J. (1978) Mesozoic-Cenozoic Cordilleran plate tectonics. In *Cenozoic tectonics and*
676 *regional geophysics of the Western Cordillera* (eds. R. B. Smith and G. P. Eaton).
677 Geological Society of America Memoir, pp. 33–50.
678 Cook N. J., Ciobanu C. L. and Mao J. (2009a) Textural control on gold distribution in As-free
679 pyrite from the Dongping, Huangtuliang and Hougou gold deposits, North China Craton
680 (Hebei Province, China). *Chem. Geol.* **264**, 101–121.
681 Cook N. J., Ciobanu C. L. and Spry P. G. (2009b) Understanding gold-(silver)-telluride-
682 (selenide) mineral deposits. *Episodes* **32**, 249–263.
683 Cooke D. R. and McPhail D. C. (2001) Epithermal Au-Ag-Te mineralization, Acupan, Baguio
684 district, Philippines: Numerical simulations of mineral deposition. Econ. Geol. **96**, 109–
685 131.
686 Deditius A. P., Utsunomiya S., Renock D., Ewing R. C., Ramana C. V., Becker U. and Kesler
687 S. E. (2008) A proposed new type of arsenian pyrite: Composition, nanostructure and
688 geological significance. *Geochim. Cosmochim. Acta* **72**, 2919–2933.
689 Deditius A. P., Utsunomiya S., Ewing R. C., Chryssoulis S. L., Venter D. and Kesler S. E.
690 (2009) Decoupled geochemical behavior of As and Cu in hydrothermal systems.
691 *Geology* **37**, 707–710.

692 Deditius A. P., Reich M., Kesler S. E., Utsunomiya S., Chryssoulis S. L., Walshe J. and Ewing
693 R. C. (2014) The coupled geochemistry of Au and As in pyrite from hydrothermal ore
694 deposits. *Geochim. Cosmochim. Acta* **140**, 644–670.
695 Deditius A. P. and Reich M. (2016) Constraints on the solubility of Hg, Tl and Cd in arsenian
696 pyrite. *Am. Mineral.* **101**, 1451–1459.
697 Drummond S. E. and Ohmoto H. (1985) Chemical evolution and mineral deposition in boiling
698 hydrothermal systems. *Econ. Geol.* **80**, 126–147.
699 Dwelley P. C. (1984) Geology, mineralization, and fluid inclusion analysis of the Ajax vein
700 system, Cripple Creek, Colorado. M.Sc. thesis, Colorado State Univ.
701 Dye M. D. (2015) Mineralogical characterization and paragenesis of the Cripple Creek deposit,
702 Colorado M.Sc. thesis, Colorado School of Mines.
703 Edmonds E., Mather T. A. and Liu E. J. (2018) A distinct metal fingerprint in arc volcanic
704 emissions. *Nat. Geosci.* **11**, 790–794.
705 Einaudi M. T., Hedenquist J. W. and Inan E. E. (2005) Sulfidation state of fluids in active and
706 extinct hydrothermal systems: Transitions from porphyry to epithermal environments.
707 In *Volcanic, geothermal, and ore-forming fluids: Rulers and witnesses of processes in*
708 *the Earth* (eds. S. F. Simmons and I. Graham). Special Publications of the Society of
709 Economic Geology, v. 10, pp. 1–50.
710 Fleet M. E. and Mumin H. (1997) Gold-bearing arsenian pyrite and marcasite and arsenopyrite
711 from Carling Trend gold deposits and laboratory synthesis. *Am. Mineral.* **82**, 182–193.
712 Gao S., Xu H., Li S., Santosh M., Zhang D., Yang L. and Quan S. (2017) Hydrothermal
713 alteration and ore-forming fluids associated with gold-tellurium mineralization in the
714 Dongping gold deposit, China. *Ore Geol. Rev.* **80**, 166–184.
715 George L., Cook N. J., Ciobanu C. L. and Wade B. P. (2015) Trace and minor elements in
716 galena: A reconnaissance LA-ICP-MS study. *Am. Mineral.* **100**, 548–569.

717 Govindaraju K. (1994) 1994 Compilation of working values and descriptions for 383
718 geostandards. *Geostandard Newslett.* **118**, 1-158.
719 Gregory D., Meffre S. and Large R. (2014) Comparison of metal enrichment in pyrite
720 framboids from a metal-enriched and metal-poor estuary. *Am. Mineral.* **99**, 633-644.
721 Gregory D. D., Large R. R., Halpin J. A., Baturina E. L., Lyons T. W., Wu S., Danyushevsky
722 L., Sack P. J., Chappaz A., Maslennikov,V. V. and Bull S. W. (2015) Trace element
723 content of sedimentary pyrite in black shales. *Econ. Geol.* **110**, 1389-1410.
724 Gregory D. D., Cracknell M. J., Large R. R., McGoldrick P., Kuhn S., Maslennikov V. V.,
725 Baker M. J., Fox N., Belousov I., Figueroa M. C., Steadman J. A., Fabris A. J. and Lyons
726 T. W. (2019) Distinguishing ore deposit type and barren sedimentary pyrite using laser
727 ablation-inductively coupled plasma-mass spectrometry trace element data and
728 statistical analysis of large data sets. *Econ. Geol.* **114**, 771-786.
729 Grundler P. V., Brugger J., Etschmann B. E., Helm L., Liu W., Spry P. G., Tian Y., Testemale
730 D. and Pring A. (2013) Speciation of aqueous tellurium (IV) in hydrothermal solutions
731 and vapors, and the role of oxidized tellurium species in Te transport and gold
732 deposition. *Geochim. Cosmochim. Acta* **120**, 298–325.
733 Holwell D. A., Fiorentini M., McDonald I., Lu Y., Giuliani A., Smith D. J., Keith M., Locmelis
734 M. (2019) A metasomatized lithospheric mantle control on the metallogenic signature
735 of post-subduction magmatism. *Nat. Comm.* **10**, 1–10.
736 Huston D. L., Sie S. H., Suter G. F., Cooke D. R. and Both R. A. (1995) Trace elements in
737 sulfide minerals from Eastern Australian volcanic-hosted massive sulfide deposits: Part
738 I. Proton microprobe analyses of pyrite, chalcopyrite and sphalerite, and part II.
739 Selenium levels in pyrite: Comparison with d34S values and implications for the source
740 of sulfur in volcanogenic hydrothermal systems. *Econ. Geol.* **90**, 1167–1196.
741 Imai N., Terashima S., Itoh S. and Ando A. (1995) 1994 compilation of analytical data for

742 minor and trace elements in seventeen GSJ geochemical reference samples, “igneous
743 rock series”. *Geostandard. Newslett. 19*, 135-213.
744 Imai N., Terashima S., Itoh S. and Ando A. (1996) 1996 compilation of analytical data of nine
745 GSJ geochemical reference samples “sedimentary rock series”. *Geostandard. Newslett.*
746 **20**, 165-216.
747 Imai N., Terashima S., Itoh S. and Ando A. (1999) 1998 compilation of analytical data for five
748 GSJ geochemical reference samples: the “instrumental analysis series”. *Geostandard.*
749 *Newslett.* **23**, p. 223-250.
750 Jenner F. E., O’Neill H. S. C., Arculus R. J. and Mavrogenes A. (2010) The magnetite crisis
751 in the evolution of arc-related magmas and the initial concentration of Au, Ag and Cu.
752 J. Petrol. **51**, 2445–2464.
753 Jenner F. E. (2017) Cumulate causes for the low contents of sulfide-loving elements in the
754 continental crust. *Nat. Geosci.* **10**, 524-529.
755 Jensen E. P. and Barton M. D. (2000) Gold deposits related to alkaline magmatism. *Rev. Econ.*
756 *Geol.* **13**, 279–314.
757 Jensen E. P. (2003) Magmatic and hydrothermal evolution of the Cripple Creek gold deposit,
758 Colorado, and comparisons with regional and global magmatic-hydrothermal systems
759 associated with alkaline magmatism. Ph.D. thesis, Univ. of Arizona.
760 Jensen E. P. and Barton M. D. (2007) Geology, petrochemistry, and time-space evolution of
761 the Cripple Creek district, Colorado. *Geol. Soc. Am.* **10**, 63–78.
762 Keith M., Haase K. M., Klemd R., Krumm S. and Strauss S. (2016a) Systematic variations of
763 trace element and sulfur isotope compositions in pyrite with stratigraphic depth in the
764 Skouriotissa volcanic-hosted massive sulfide deposit, Troodos ophiolite, Cyprus. *Chem.*
765 *Geol.* **423**, 7–18.
766 Keith M., Häckel F., Haase K. M., Schwarz-Schampera U. and Klemd R. (2016b) Trace

element systematics of pyrite from submarine hydrothermal vents. *Ore Geol. Rev.* **72**, 728–745.

Keith M., Haase K. M., Klemd R., Schwarz-Schampera U. and Franke H. (2017) Systematic variations in magmatic sulphide chemistry from mid-ocean ridge, back-arc and island arcs. Chem. Geol. **451**, 67–77.

Keith M., Smith D. J., Jenkin G. R. T., Holwell D. A. and Dye M. D. (2018a) A review of Te and Se systematics in hydrothermal pyrite from precious metal deposits: Insights into ore-forming processes. *Ore Geol. Rev.* **96**, 269–282.

Keith M., Haase K. M., Klemd R., Smith D. J., Schwarz-Schampera U. and Bach W. (2018b) Constraints on the source of Cu in a submarine magmatic-hydrothermal system, Brothers volcano, Kermadec island arc. *Contrib. Mineral. Petrol.* **173**, 1–16.

Kelley K. D., Romberger S. B., Beaty D. W., Pontius J. A., Snee L. W., Stein H. J. and Thompson T. B. (1998) Geochemical and geochronological constraints on the genesis of Au-Te deposits at Cripple Creek, Colorado. *Econ. Geol.* **93**, 981–1012.

Kelley K. D. and Ludington S. (2002) Cripple Creek and other alkaline-related gold deposits in the southern Rocky Mountains, USA: influence of regional tectonics: *Mineral. Deposita* **37**, 38–60.

Kelley K. D. and Spry P. G. (2016) Critical Elements in Alkaline Igneous Rock-Related Epithermal Gold Deposits. *Econ. Geol.* **18**, 195–216.

Kesler S. E., Deditius A. P. and Chryssoulis S. (2007) Geochemistry of Se and Te in arsenian pyrite: new evidence for the role of Se and Te hydrothermal complexes in Carlin and epithermal-type deposits. In Au–Ag–Te–Se deposits: Espo, Finnland (eds. K. K. Kojonen, N. J. Cook and V. J. Ojala). Proceedings of the 2007 Field Workshop, Geological Survey of Finland, v. 53, pp. 85–95.

Liu W. H., Borg S. J., Testemale D., Etschmann B., Hazemann J. L. and Brugger J. (2011)

792 Speciation and thermodynamic properties for cobalt chloride complexes in hydrothermal
793 fluids at 35-440° C and 600 bar: An in-situ XAS study. *Geochim. Cosmochim Acta* **75**,
794 1227-1248.
795 Martin A. J., Keith M., McDonald I., Haase K. M., McFall K. A., Klemd R. and MacLeod C.
796 J. (2019) Trace element systematics and ore-forming processes in mafic VMS deposits:
797 Evidence from the Troodos ophiolite, Cyprus. *Ore Geol. Rev.* **106**, 205-225.
798 Maslennikov V. V., Maslennikova S. P., Large R. R. and Danyushevsky L. V. (2009) Study
799 of trace element zonation in vent chimneys from the Silurian Yaman-Kasy volcanic-
800 hosted massive sulphide deposit (Southern Urals, Russia) using Laser Ablation-
801 Inductively Coupled Plasma Mass Spectrometry (LA-ICPMS). *Econ. Geol.* **104**, pp.
802 1111–1141.
803 McPhail D. C. (1995) Thermodynamic properties of aqueous tellurium species between 25
804 and 350°C. *Geochim. Cosmochim. Acta* **59**, 851–866.
805 Pals D. W. and Spry P. G. (2003) Telluride mineralogy of the low-sulfidation epithermal
806 Emperor gold deposit, Vatukoula, Fiji: *Miner. Petrol.* **79**, 285–307.
807 Pals D. W., Spry P. G. and Chryssoulis S. (2003) Invisible Gold and Tellurium in Arsenic-
808 Rich Pyrite from the Emperor Gold Deposit, Fiji: Implications for Gold Distribution and
809 Deposition. *Econ. Geol.* **98**, 479–493.
810 Patten C., Barnes S.-J., Mathez E. A. and Jenner F. E. (2013) Partition coefficients of
811 chalcophile elements between sulfide and silicate melts and the early crystallization
812 history of sulfide liquid: LA-ICP-MS analysis of MORB sulfide droplets. *Chem. Geol.*
813 **358**, 170–188.
814 Pokrovski G. S., Zakirov I. V., Roux J., Testemale D., Hazemann J.-L., Bychkov A. Y. and
815 Golikova G. V. (2002) Experimental study of arsenic speciation in vapor phase to 500°C:
816 Implications for As transport and fractionation in low-density crustal fluids and volcanic

gases. *Geochim. Cosmochim. Acta* **66**, 3453–3480.

Pokrovski G. S., Borisova A. Y. and Harrichoury J.-C. (2008) The effect of sulfur on vapor-liquid fractionation of metals in hydrothermal systems. *Earth Planets Sci. Lett.* **266**, 345–362.

Pokrovski G. S., Borisova A. Y. and Bychkov, A. Y., 2013, Speciation and transport of metals and metalloids in geological vapors. *Rev. Mineral. Geochem.* **76**, 165–218.

Pokrovksi G. S., Kokh M. A., Proux O., Hazemann J. L., Bazarkina E. F., Testemale D., Escoda C., Boiron M. C., Blanchard M., Aigouy T., Gouy S., de Parseval P. and Thibaut M. (2019) The nature and partitioning of invisible gold in the pyrite-fluid system. *Ore Geol. Rev.* **109**, 545-563.

Pudack C., Halter W. E., Heinrich C. A. and Petke T. (2009) Evolution of magmatic vapor to gold-rich epithermal liquid: The porphyry to epithermal transition at Nevados de Famatina, Northwest Argentina. *Econ. Geol.* **104**, 449–477.

Rampe J. S., Geissman J. W., Melker M. D. and Heizler M. T. (2005) Paleomagnetic and geochronologic data bearing on the timing, evolution, and structure of the Cripple Creek diatreme complex and related rocks, Front Range, Colorado. *Geophysical Monograph Series* **154**, 107-123.

Reimann C. and Filzmoser P. (2000) Normal and lognormal data distribution in geochemistry: Death of a myth. Consequences for the statistical treatment of geochemical and environmental data: *Environ. Geol.* **39**, 1001-1014.

Reed M. H. and Palandri J. (2006) Sulfide mineral precipitation from hydrothermal fluids: *Rev. Mineral. Geochem.* **61**, 609–631.

Reich M., Kesler S. E., Utsunomiya S., Palenik C. S., Chryssoulis S. L. and Ewing R. C. (2005) Solubility of gold in arsenian pyrite. *Geochim. Cosmochim. Acta* **69**, 2781–2796.

Reich M., Deditius A. P., Chryssoulis S., Li J.-W., Ma C.-Q., Parada M. A., Barra F. and

842 Mittermayr F. (2013) Pyrite as a record of hydrothermal fluid evolution in a porphyry
843 copper system: A SIMS/EMPA trace element study. *Geochim. Cosmochim. Acta* **104**,
844 42–62.
845 Richards J. R. and Kerrich R. (1993) The Porgera Gold mine, Papua New Guinea: Magmatic
846 Hydrothermal to Epithermal Evolution of an Alkalic-type Precious Metal Deposit. *Econ.*
847 *Geol.* **88**, 1017–1052.
848 Richards J. P. (2011) Magmatic to hydrothermal metal fluxes in convergent and collided
849 margins. *Ore Geol. Rev.* **40**, 1-26.
850 Rock N. M. S. and Groves D. I. (1988) Do lamprophyres carry gold as well as diamonds?
851 *Nature* **332**, 253-255.
852 Román N., Reich M., Leisen M., Morata D., Barra F. and Deditius A. P. (2019) Geochemical
853 and micro-textural fingerprints of boiling in pyrite. *Geochim. Cosmochim. Acta* **264**, 60-
854 85.
855 Ronacher E., Richards J. P., Reed M. H., Bray C. J., Spooner E. T. C. and Adams P. D. (2004)
856 Characteristics and evolution of the hydrothermal fluid in the north zone high-grade area,
857 Porgera gold deposit, Papua New Guinea. *Econ. Geol.* **99**, 843–867.
858 Saunders J. A. (1986) Petrology, mineralogy, and geochemistry of representative gold telluride
859 ores from Colorado. Ph.D. thesis, Colorado School of Mines.
860 Savage K. S., Tingle T. N., O'Day P. A., Waychunas A. and Bird D. K. (2000) Arsenic
861 speciation in pyrite and secondary weathering phases, Mother Load Gold District,
862 Tuolumne County, California. *Appl. Geochem.* **15**, 1219–1244.
863 Schirmer T., Koschinsky A. and Bau M. (2014) The ratio of tellurium and selenium in
864 geological material as a possible paleo-redox proxy. *Chem. Geol.* **376**, 44–51.
865 Sillitoe R. H. (2002) Some metallogenic features of gold and copper deposits related to
866 alkaline rocks and consequences for exploration. *Mineral. Deposita* **37**, 4–13.

867 Simmons S. F., White N. C., John D. A. (2005) Geological characteristics of epithermal
868 precious and base metal deposits. *Econ. Geol.* **100**, 485–522.
869 Smith D. J., Naden J., Jenkin G. R. T. and Keith M. (2017) Hydrothermal alteration and fluid
870 pH in alkaline-hosted epithermal systems. *Ore Geol. Rev.* **89**, 772–779.
871 Seyfried W. E. and Ding K. (1995) Phase equilibria in subseafloor hydrothermal systems: A
872 review of the role of redox, temperature, pH and dissolved Cl on the chemistry of hot
873 spring fluid at mid-ocean ridges. In *Seafloor hydrothermal systems, physical, chemical,*
874 *biological and geological interactions* (eds. S. R. Humphris, R. A. Zierenberg, L. S.
875 Mullineaux and R. E. Thomson). Geophysical Monograph Series, v. 91, pp. 248–272.
876 Seyfried W. E., Ding K., Berndt M. E. and Chen X. (1999) Experimental and theoretical
877 controls on the composition of mid-ocean ridge hydrothermal fluids. Rev. *Econ. Geol.*
878 **8**, 181-200.
879 Spry P. G. and Scherbarth N. L. (2006) The gold-vanadium-tellurium association at the Tuvatu
880 gold-silver prospect, Fiji: conditions of ore deposition. *Mineral. Petrol.* **87**, 171–186.
881 Tardani D., Reich M., Deditius A. P., Chryssoulis S., Sánchez-Alfaro P., Wrage J. and Roberts
882 M. P. (2017) Copper-arsenic decoupling in an active geothermal system: A link between
883 pyrite and fluid composition. *Geochim. Cosmochim. Acta* **204**, 179–204.
884 Thompson T. B., Trippel A. D. and Dwelley P. C. (1985) Mineralized veins and breccia of the
885 Cripple Creek district, Colorado. *Econ. Geol.* **80**, 1669–1688.
886 Wallier S., Rey R., Kouzmanov K., Pettke T., Heinrich C. A., Leary S., O'Connor G., Tamas
887 C. G., Vennemann T., Ullrich T. (2006) Magmatic fluids in the breccia-hosted
888 epithermal Au-Ag deposit of Rosia Montana, Romania. *Econ. Geol.* **101**, 923–954.
889 Wedepohl K. H. (1995) The composition of the continental crust. *Geochim. Cosmochim. Acta*
890 **59**, 1217–1232.
891 Whitney D. L. and Evans B. W. (2010) Abbreviations for names of rock-forming minerals.

892 *Am. Mineral.* **95**, 185-187.
893 Williams-Jones A. E. and Heinrich C. A. (2005) Vapor transport or metals and the formation
894 of magmatic-hydrothermal ore deposits. *Econ. Geol.* **100**, 1287–1312.
895 Wohlgemuth-Ueberwasser C. C., Viljoen F., Petersen S. and Vorster C. (2015) Distribution
896 and solubility limits of trace elements in hydrothermal black smoker sulfides: An in-situ
897 LA-ICP-MS study. *Geochim. Cosmochim. Acta* **159**, 16–41.
898 Zajacz Z., Seo J. H., Candela P. A., Piccoli P. M., Heinrich C. A. and Guillong M. (2010)
899 Alkali metals control the release of gold from volatile-rich magmas. *Earth Planet. Sci.*
900 *Lett.* **297**, 50-56.
901 Zajacz Z., Candela P. A., Piccoli P. M., Sanchez-Valle C., Wälle M. (2013) Solubility and
902 partitioning behavior of Au, Cu, Ag and reduced S in magmas. *Geochim. Cosmochim.*
903 *Acta* **112**, 288-304.
904 Zajacz, Z., Candela, P. A. and Piccoli, P. M. (2017) The partitioning of Cu, Au and Mo
905 between liquid and vapor at magmatic temperatures and its implications for the genesis
906 of magmatic-hydrothermal ore deposits. *Geochim. Cosmochim. Acta* **207**, 81-101.
907 Zhang X. and Spry P. G. (1994) Calculated stability of aqueous tellurium species, calaverite
908 and hessite at elevated temperatures. *Econ. Geol.* **89**, 1152–1166.

909 **Figure and table captions**

910 Fig. 1. Geological map of the lithological units and sample localities including (1) WHEX, (2)
911 Cresson (Ruby stockpile) and (3) Vindicator Valley in the Cripple Creek epithermal complex.
912 Modified after Jensen (2003). (Figures in color can be found in the web version of the article)

913 Fig. 2. Multi-element diagram comparing trace element concentrations in low-grade host rock
914 and high-grade vein-type ores with pyrite, sphalerite and galena. Concentrations normalized to

915 bulk continental crust (Wedepohl, 1995). (Figures in color can be found in the web version of
916 the article)

917 Fig. 3. Paragenetic sequence of ore-formation in the Cripple Creek epithermal deposit.
918 Abundances estimated by optical and electron microscopy. The pyrite paragenesis includes: py
919 1 (stage 1), py 2 (stage 3), py 3 (stage 3 and 4), py 4 (stage 5) and py 5 (stage 7). The presented
920 paragenetic sequence considers the results of previous studies (e.g., Dye, 2015).

921 Fig. 4. Photomicrographs of representative low-grade ore samples from Cripple Creek in
922 reflected light: (A) BMS mineralization hosted in the volcanic breccia, (B) association of
923 dissolved py 2 and euhedral/dense py 3, (C) galena and sphalerite post-dating py 3, (D)
924 tennantite inclusion in sphalerite, (E) pyrrhotite inclusion in py2/3, (F) rutile replacing py 2/3.
925 Note the less euhedral shape of py 3 in (C) and (D) compared to (B), which may be related to
926 py 3 replacement by the onset of the galena and sphalerite precipitation. (Figures in color can
927 be found in the web version of the article)
928 Abbreviations (cf. Whitney and Evans, 2010): gn = galena, po = pyrrhotite, py = pyrite, sp =
929 sphalerite, tnt = tennantite.

930 Fig. 5. Representative electron images of ore samples from Cripple Creek in back-scattered
931 electron mode: (A) calaverite ($AuTe_2$) post-dating py 4 in the high-grade ore, (B) inclusions of
932 hessite (Ag_2Te), monazite, native Ag and sphalerite in py 3 in the low-grade ore, (C)
933 chalcopyrite and galena in py 3 in the low-grade ore, (D) association of calaverite ($AuTe_2$) and
934 petzite (Ag_3AuTe_2) in the high-grade ore.
935 Abbreviations (cf. Whitney and Evans, 2010): clv = calaverite, ccp = chalcopyrite, gn = galena,
936 hes = hessite, mnz = monazite, ptz = petzite, py = pyrite, sp = sphalerite.

937 Fig. 6. Back-scattered electron image (A) and major element mapping by EDS (B to D) of a
938 calaverite ($AuTe_2$) - altaite (PbTe) assemblage hosted in the high-grade vein-type ore. (Figures
939 in color can be found in the web version of the article)
940 Abbreviations: alt = altaite, clv = calaverite.

941 Fig. 7. Back-scattered electron image (A) and major element mapping by EDS (B to D)
942 displaying the complex relationship between calaverite ($AuTe_2$), coloradoite (HgTe) and native
943 Au in the high-grade quartz-fluorite veins. The white arrow in (B) displays the suggested
944 paragenetic relationship (cf. Fig. 3). The high Te intensities in fluorite (B) and Hg in calaverite
945 and native Au (D) are due to the Te Lα - Ca Kα and Au Mα and Hg Mα peak overlap,
946 respectively. (Figures in color can be found in the web version of the article)
947 Abbreviations: clv = calaverite, col = coloradoite, Au = native Au, fl = fluorite, qtz = quartz.

948 Fig. 8. Major element variation diagrams of pyrite with low Te/As (grey diamonds) and high
949 Te/As ratios (white diamonds, cf. Fig. 10B): (A) As-S and (B) As-Fe. Note the negative
950 correlation of As and S in pyrite.

951 Fig. 9. Trace element maps by LA-ICP-MS of py 3 in low-grade ores from Vindicator Valley
952 (A to F) and Ruby (G to L). The presented values are the concentrations (in ppm) of the
953 corresponding trace element in the mapped area obtained by previous spot analyses. The white
954 dashed lines are used to highlight certain zones in py 3 (B) or reflect the crystal margin. (Figures
955 in color can be found in the web version of the article)
956 Abbreviations: BDL = below detection limit.

957 Fig. 10. Trace element variation diagrams of pyrite with low Te/As (grey diamonds) and high
958 Te/As ratios (white diamonds) for (A) Au and (B) Te vs. As. Red and green circles refer to the
959 spot analyses in the mapped areas of py 3 in low-grade ore from Vindicator Valley and Ruby,
960 respectively (Fig. 9). The grey dashed lines represent the solubility limits for Au (A) and Te

(B) as a function of As in pyrite (Reich et al., 2005; Keith et al., 2018a). The capital letters A to E (in 10B) refer to the time-resolved LA-ICP-MS spectra of the corresponding spots, as presented in Figure 11. The grey and black solid lines are the best fit regression lines for pyrite with low and high Te/As ratios, respectively. Note that all data points above the Au solubility line refer to py 4 from Ruby, which is hosted in the high-grade veins, and therefore occurs in association with the Au-Te mineralization (Fig. 3). (Figures in color can be found in the web version of the article)

Fig. 11. Time-resolved LA-ICP–MS depth profiles for spot analyses of S, As, Ag, Te, Au, Pb and Bi of pyrite hosted in low-grade ores from Ruby (A, B), WHEX (D) and Vindicator Valley (C, E). The presented trace element profiles from Ruby (A) and Vindicator Valley (E) refer to the analyzed spots showing Te concentrations of 2.63 and 36.1, respectively, in the mapped areas of py 3 (Fig. 9B, H). Note that all laser ablation spectra are marked in Figure 10B in the bivariate Te-As system (capital letters, A to E). (Figures in color can be found in the web version of the article)

Fig. 12. Trace element variation diagrams of pyrite with low (grey diamonds) and high Te/As ratios (white diamonds, cf. Fig. 10B) for (A) Au (B) Ag, (C) Pb and (D) Bi vs. Te. Red and green circles refer to the spot analyses in the mapped areas of py 3 in the low-grade ore from Vindicator Valley and Ruby, respectively (Fig. 9). The grey and black solid lines are the best fit regression lines for pyrite with low and high Te/As, respectively. The black dashed lines represent the compositional range of common tellurides based on their Te/Au (A), Te/Ag (B), Te/Pb (C) and Te/Bi (D) ratios including, for example, calaverite (Te/Au = 0.8), petzite (Te/Au = 1.3, Te/Ag= 0.8), hessite (Te/Ag=1.7), tsumoite (Te/Bi = 0.6) and altaite (Te/Pb = 0.6). Pearson correlation coefficients (linear R values) between Te and other trace elements in pyrite can be found in the electronic supplement (Table A8). The purple and brown fields represent

985 the compositional variation of the high-grade and low-grade bulk ores, respectively. (Figures
986 in color can be found in the web version of the article)

987 Fig. 13. Flowchart summarizing the magmatic-hydrothermal mineralization processes of Te
988 and Au at Cripple Creek. Sections referred to in the figure provide details to the corresponding
989 processes. (Figures in color can be found in the web version of the article)
990 Abbreviations (cf. Whitney and Evans, 2010): Au = native Au, clv = calaverite, col =
991 coloradoite, py = pyrite.

992 Table 1. Compilation of low- and high-grade bulk ore and pyrite trace element data from the
993 investigated sites in the Cripple Creek deposit. The whole data set can be found in the electronic
994 supplement (Table A2, A3 and A6). (n = number of measurements, SD= standard deviation).

995

996

997

998

999

1000

1001

1002

1003

1004

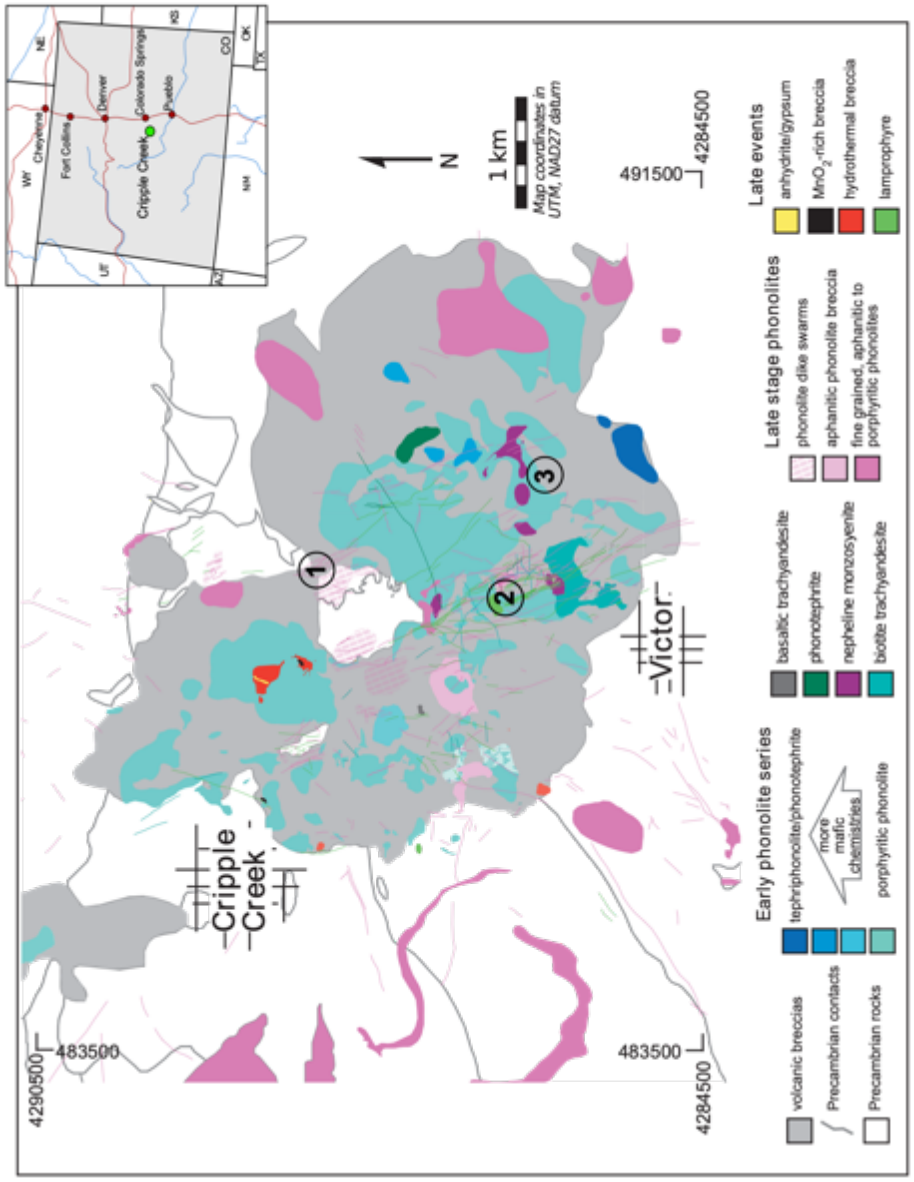
Cripple Creek
Victor
1
2
3
N
1 km
Map coordinates in UTM, NAD27 datum
491500
4284500
483500
4290500
483500
4284500
Late events
anhydrite/gypsum
MnO2-rich breccia
hydrothermal breccia
lamprophyre
Late stage phonolites
phonolite dike swarms
aphanitic phonolite breccia
fine grained, aphanitic to porphyritic phonolites
basaltic trachyandesite
phonolephrite
nepheline monzosyenite
biotite trachyandesite
Early phonolite series
tephriphonolite/phonotephrite
more mafic chemistries
porphyritic phonolite
volcanic breccias
Precambrian contacts
Precambrian rocks
WY
NE
CO
KS
OK
TX
NM
AZ
UT
Cheyenne
Fort Collins
Denver
Colorado Springs
Pueblo
Cripple Creek

Fig. 1

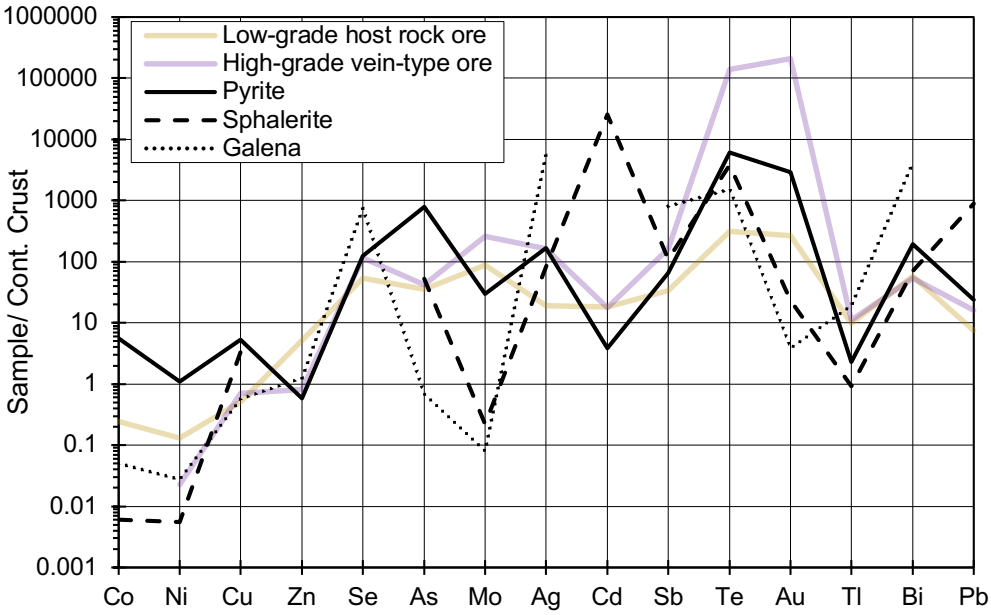
Low-grade host rock ore
High-grade vein-type ore
Pyrite
Sphalerite
Galena
Sample/ Cont. Crust
1000000
100000
10000
1000
100
10
1
0.1
0.01
0.001
Co
Ni
Cu
Zn
Se
As
Mo
Ag
Cd
Sb
Te
Au
Tl
Bi
Pb

Fig. 2

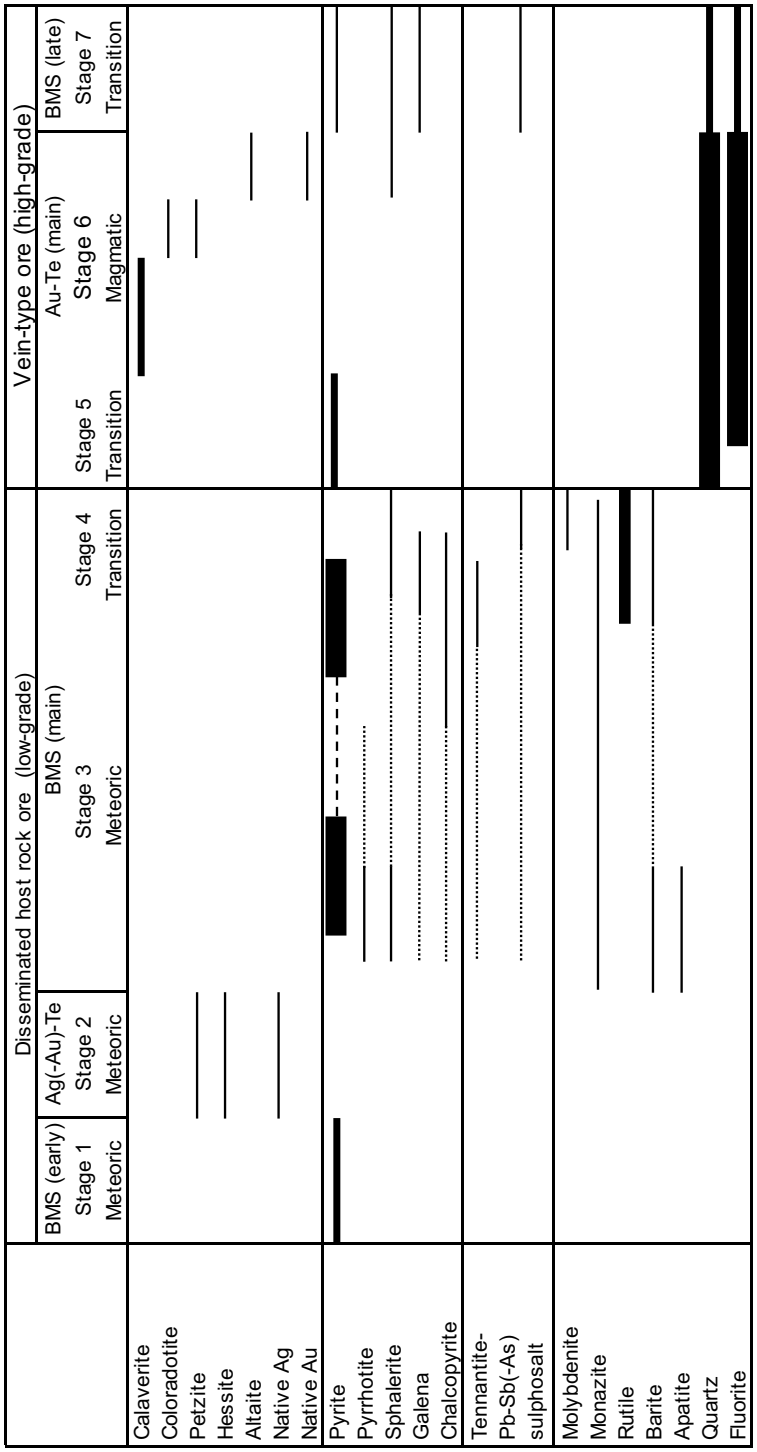
Disseminated host rock ore (low-grade)
Vein-type ore (high-grade)
BMS (early) Stage 1 Meteoric
Ag(-Au)-Te Stage 2 Meteoric
BMS (main) Stage 3 Meteoric
Stage 4 Transition
Stage 5 Transition
Au-Te (main) Stage 6 Magmatic
BMS (late) Stage 7 Transition
Calaverite
Coloradotite
Petzite
Hessite
Altaite
Native Ag
Native Au
Pyrite
Pyrrhotite
Sphalerite
Galena
Chalcopyrite
Tennantite-Pb-Sb(-As) sulphosalt
Molybdenite
Monazite
Rutile
Barite
Apatite
Quartz
Fluorite
Trace
Minor
Common
Abundant
Dominant
Dissolution
Infered
<1 %
1-5 %
5-25 %
25-50 %
>50 %

Fig. 3

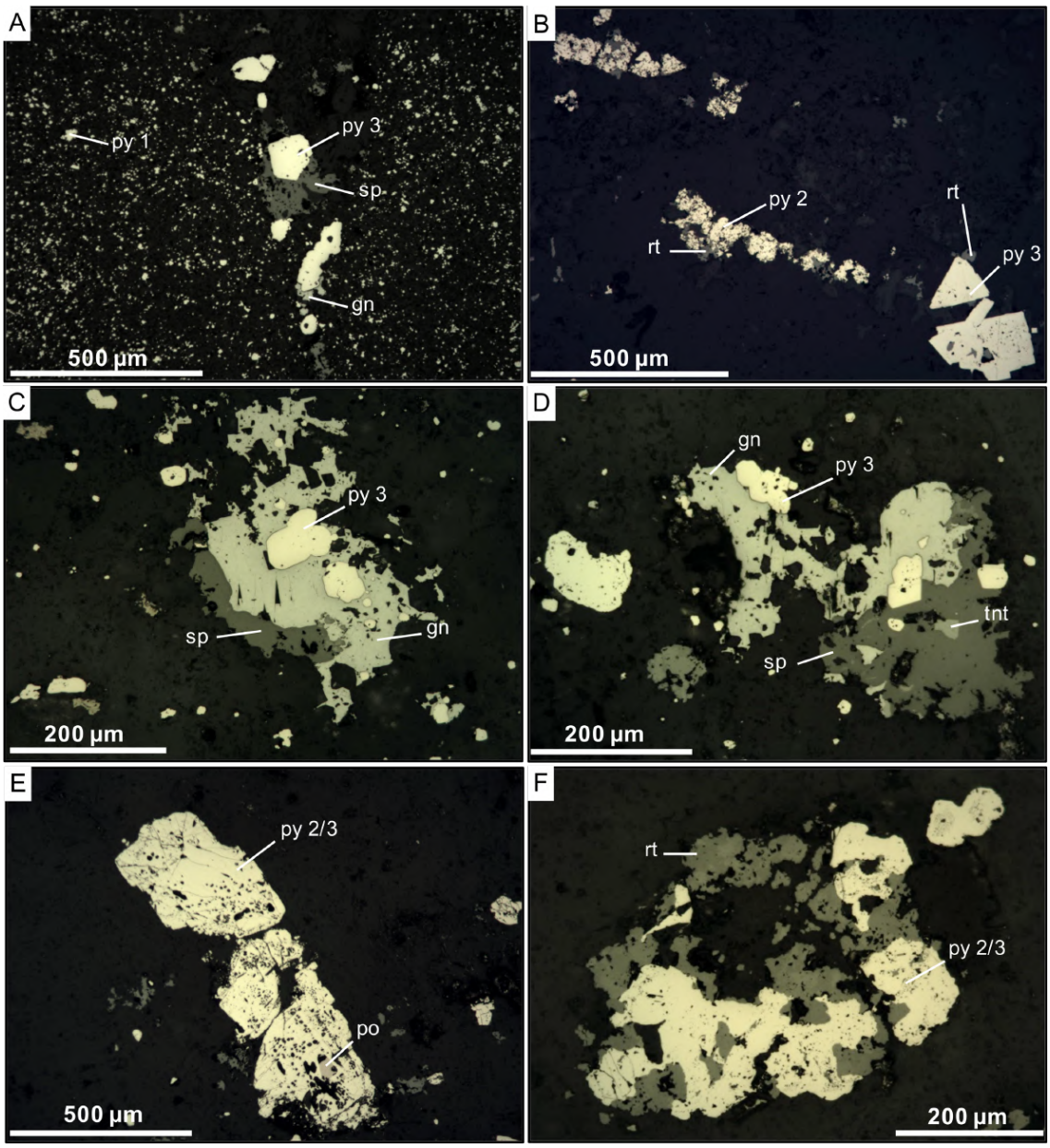
A
py 1
py 3
sp
gn
500 µm
B
py 2
rt
rt
py 3
500 µm
C
py 3
sp
gn
200 µm
D
gn
py 3
tnt
sp
200 µm
E
py 2/3
po
500 µm
F
rt
py 2/3
200 µm

Fig. 4

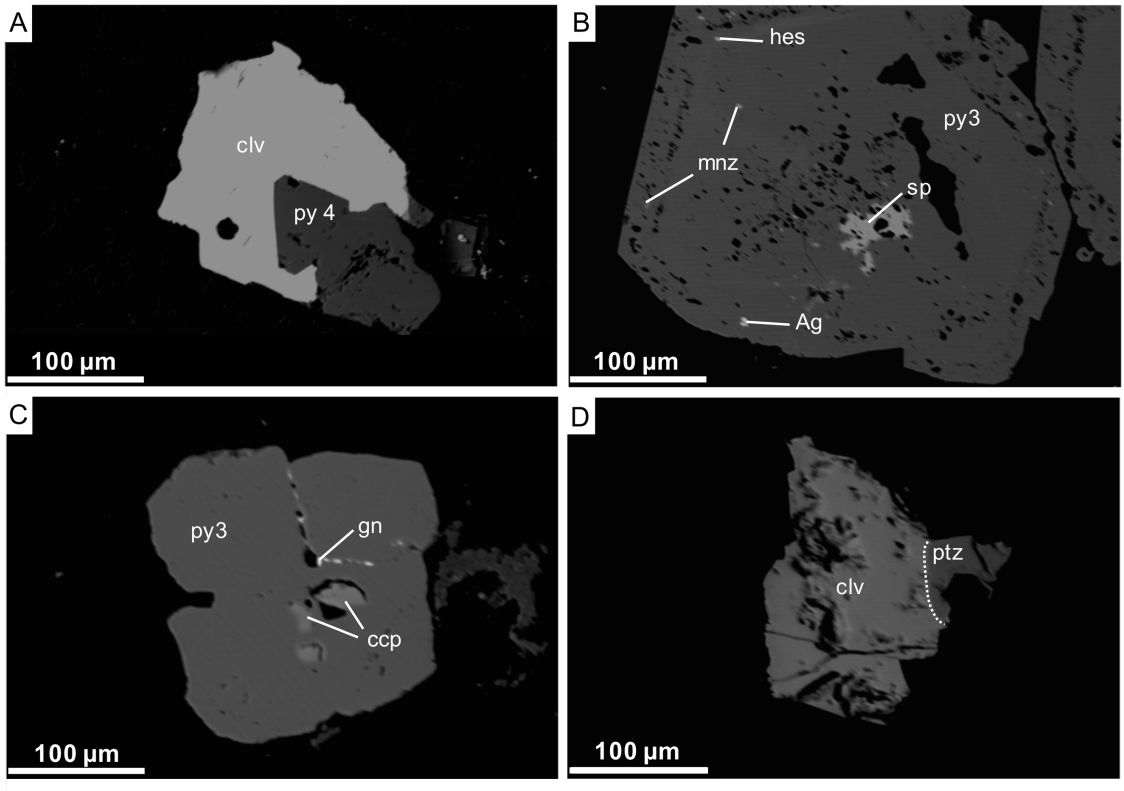
A
clv
py 4
100 µm
B
hes
py3
mnz
sp
Ag
100 µm
C
py3
gn
ccp
100 µm
D
ptz
clv
100 µm

Fig. 5

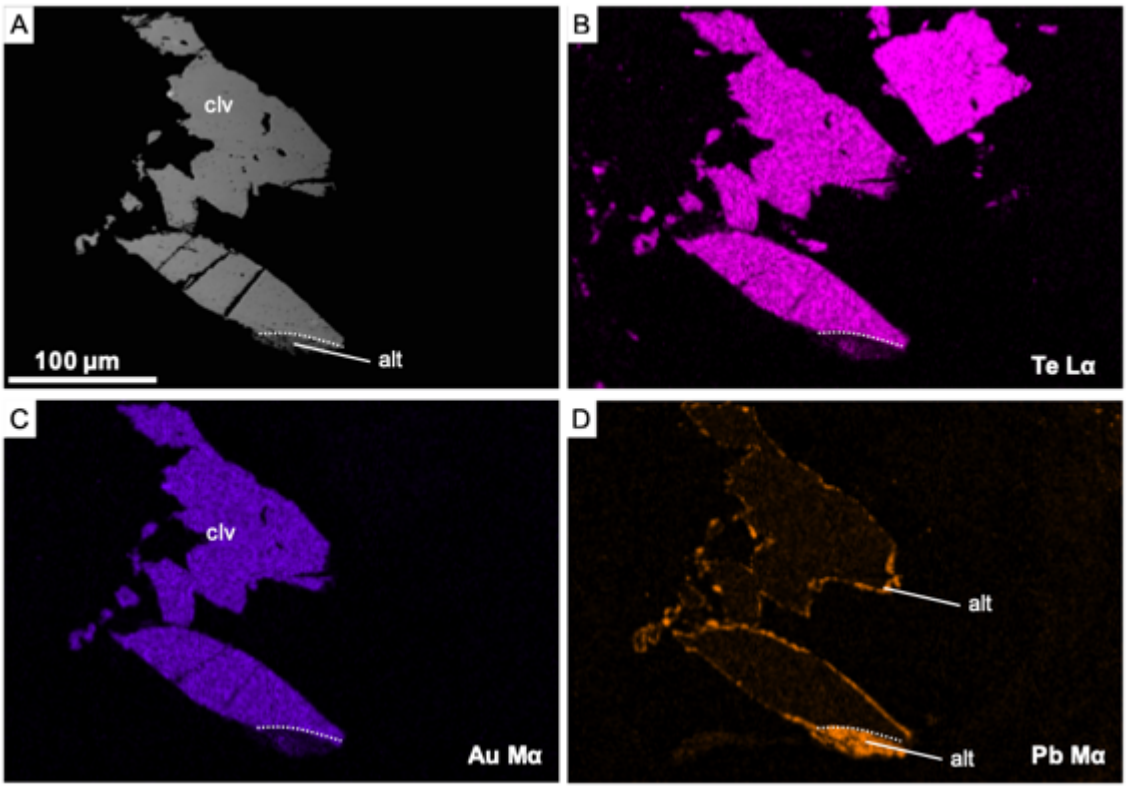

Fig. 6

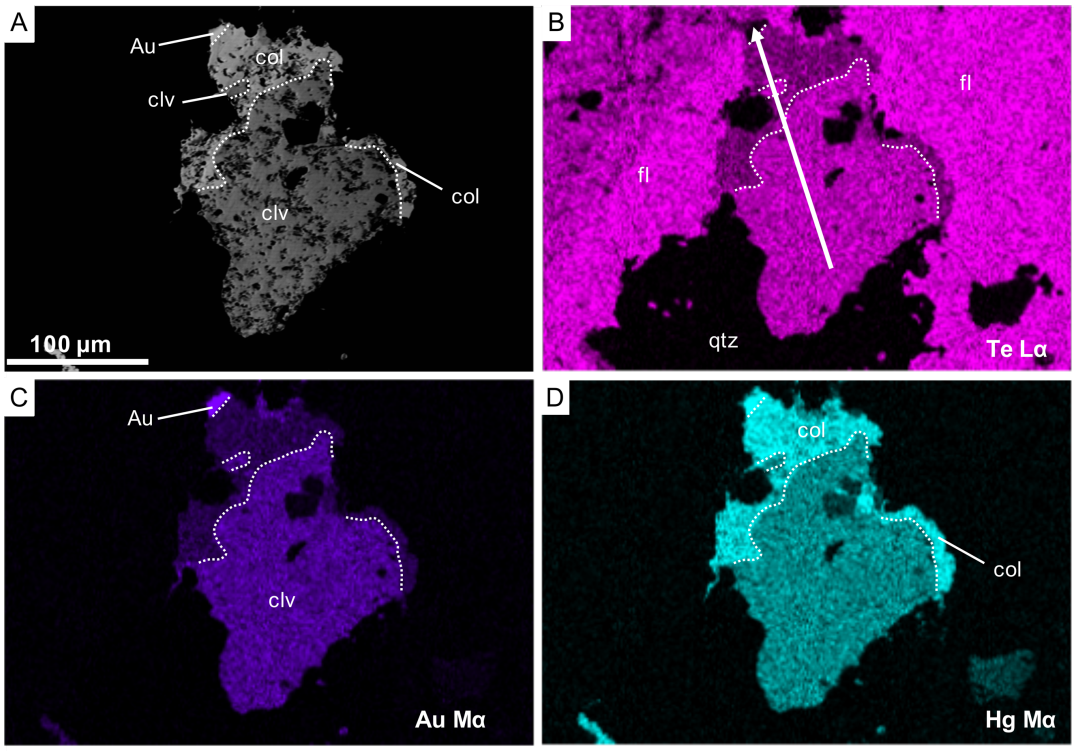
A
Au
col
clv
clv
col
100 µm
B
fl
fl
qtz
Te Lα
C
Au
clv
Au Mα
D
col
col
Hg Mα

Fig. 7

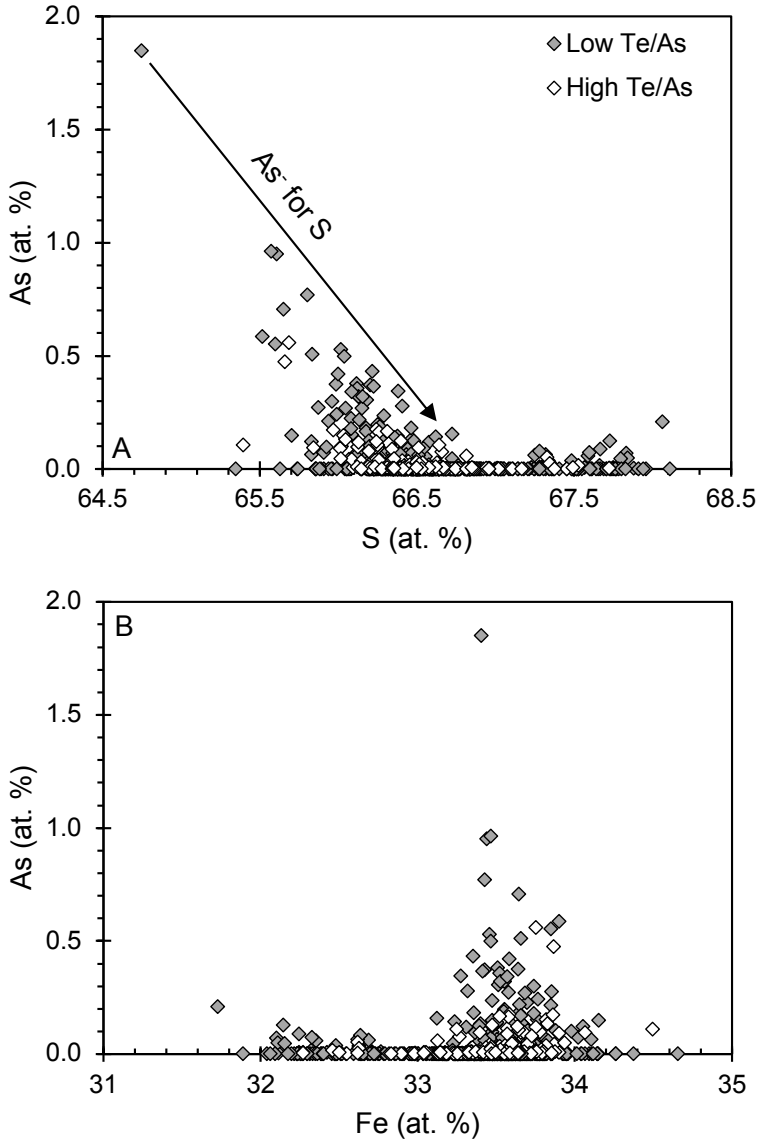
Low Te/As
High Te/As
As for S
A
As (at. %)
S (at. %)
2.0
1.5
1.0
0.5
0.0
64.5
65.5
66.5
67.5
68.5
B
As (at. %)
Fe (at. %)
31
32
33
34
35

Fig. 8

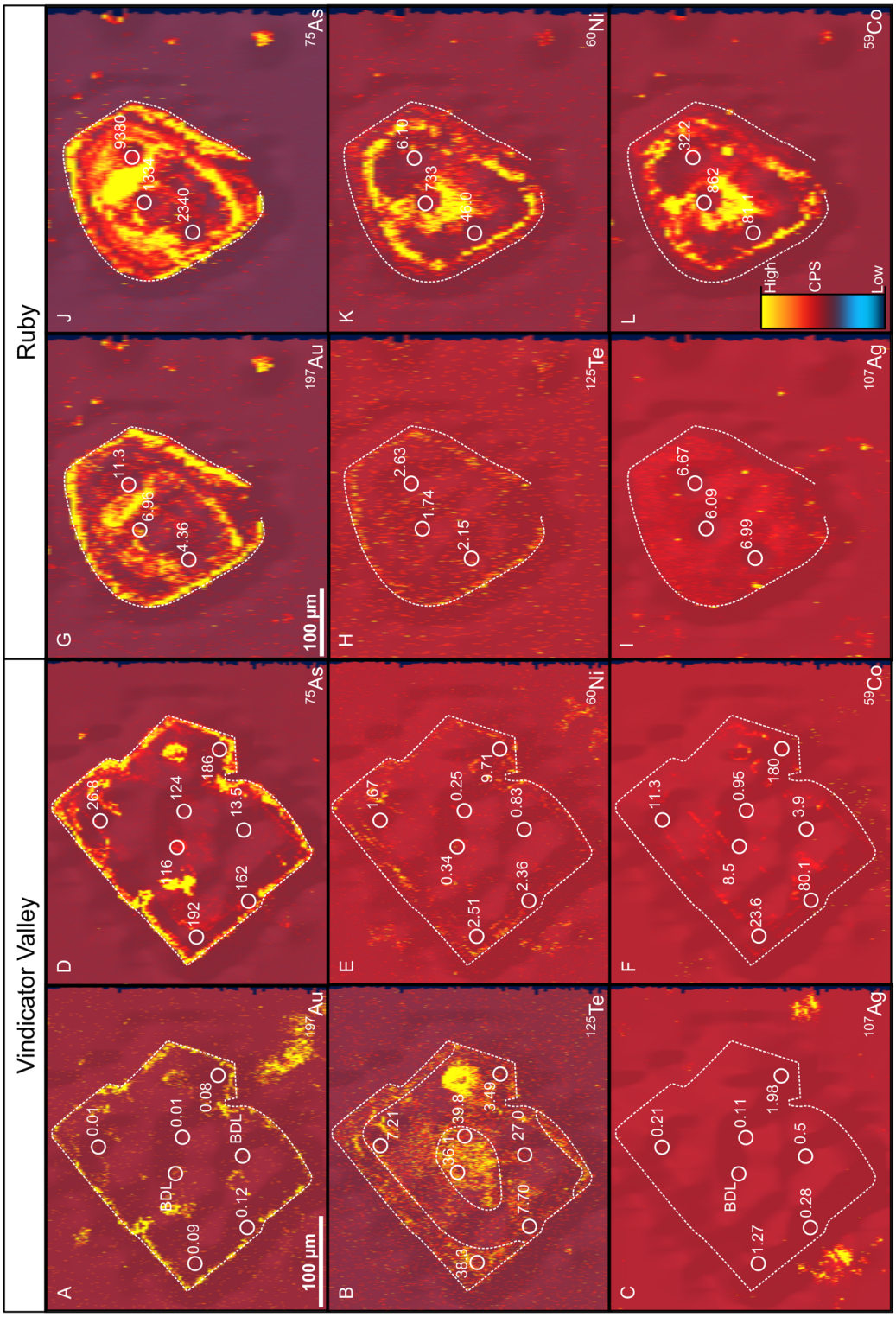
Vindicator Valley
Ruby
A
B
C
D
E
F
G
H
I
J
K
L
197Au
125Te
107Ag
75As
60Ni
59Co
100 µm
High
CPS
Low

Fig. 9

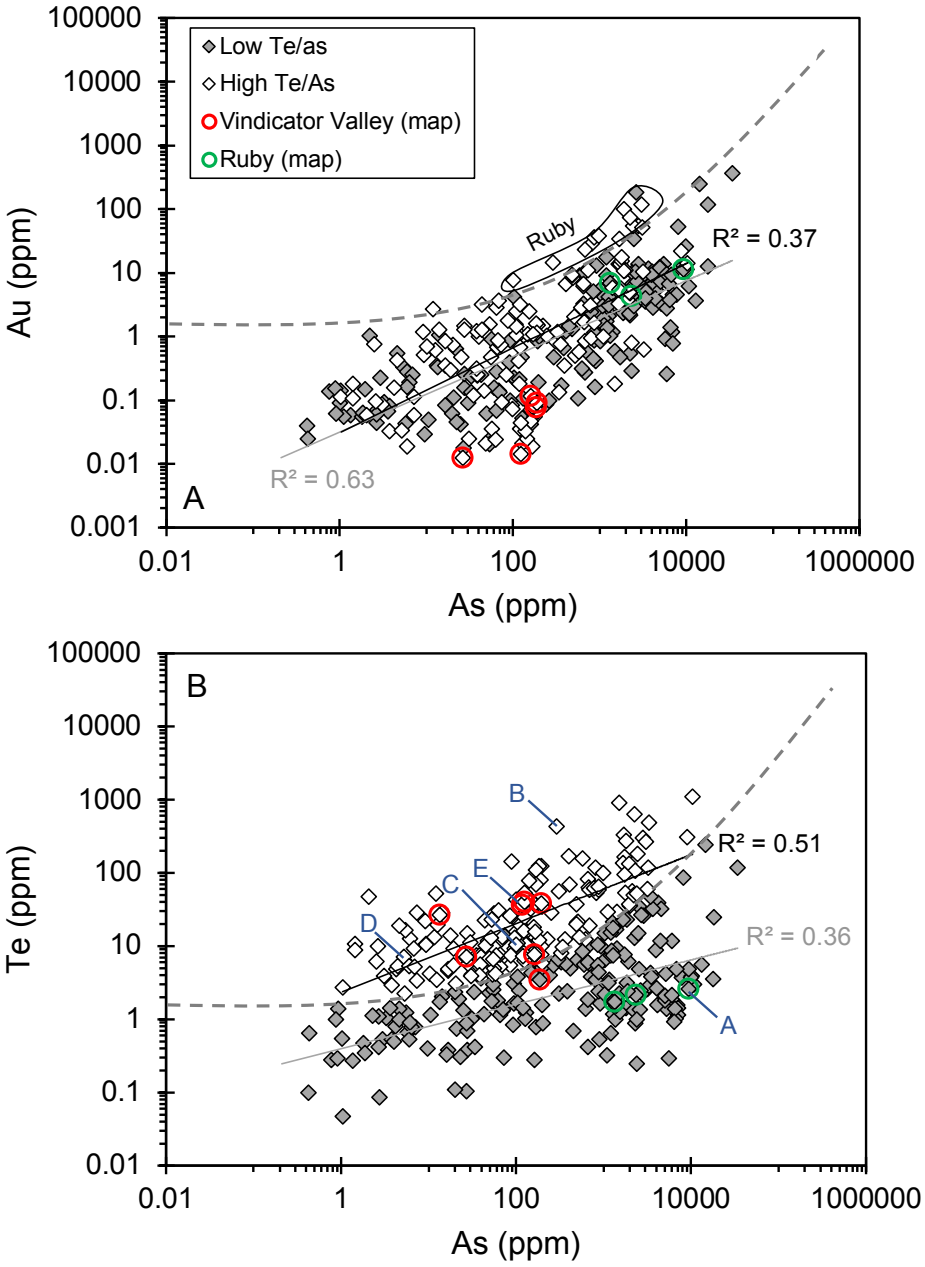
Low Te/as
High Te/As
Vindicator Valley (map)
Ruby (map)
Ruby
R² = 0.37
R² = 0.63
A
Au (ppm)
As (ppm)
100000
10000
1000
100
10
1
0.1
0.01
0.001
0.01
1
100
10000
1000000
B
R² = 0.51
R² = 0.36
B
E
C
D
A
Te (ppm)
As (ppm)

Fig. 10

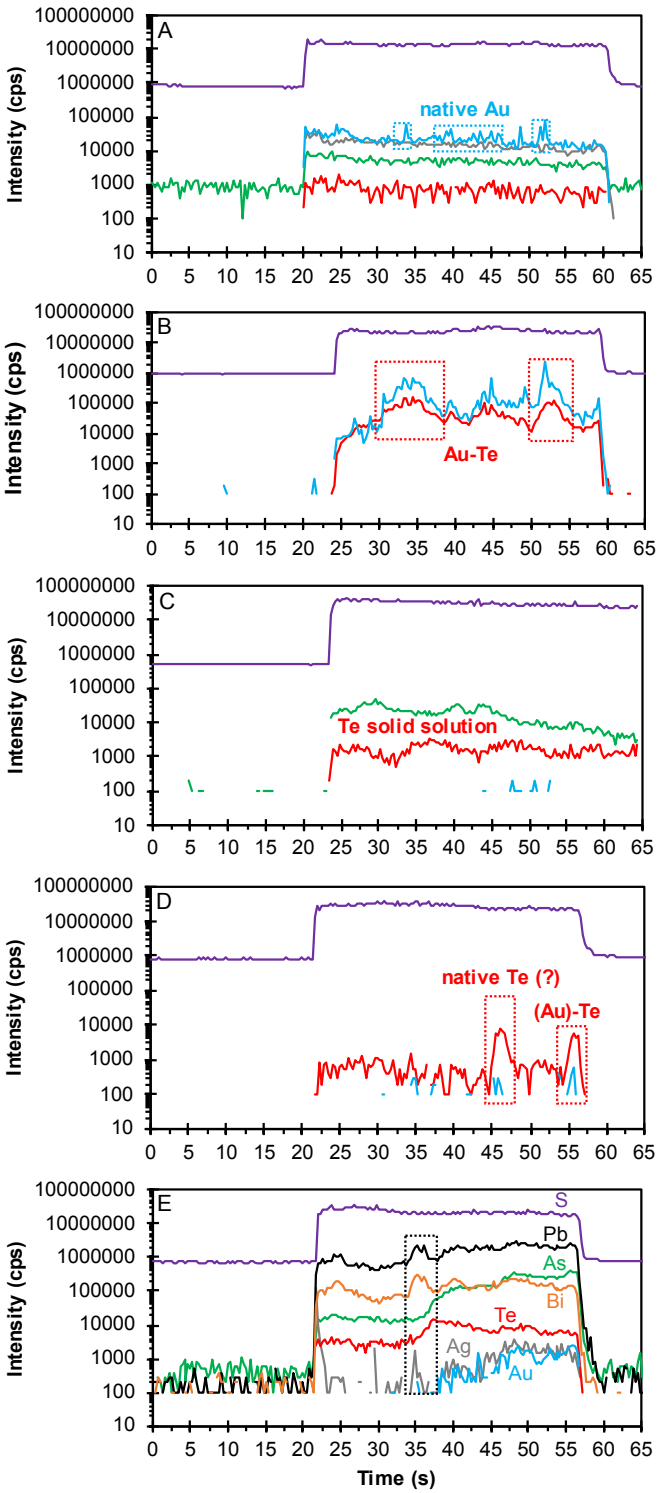
A
native Au
B
Au-Te
C
Te solid solution
D
native Te (?)
(Au)-Te
E
S
Pb
As
Bi
Te
Ag
Au
Intensity (cps)
Time (s)

1105

Fig. 11

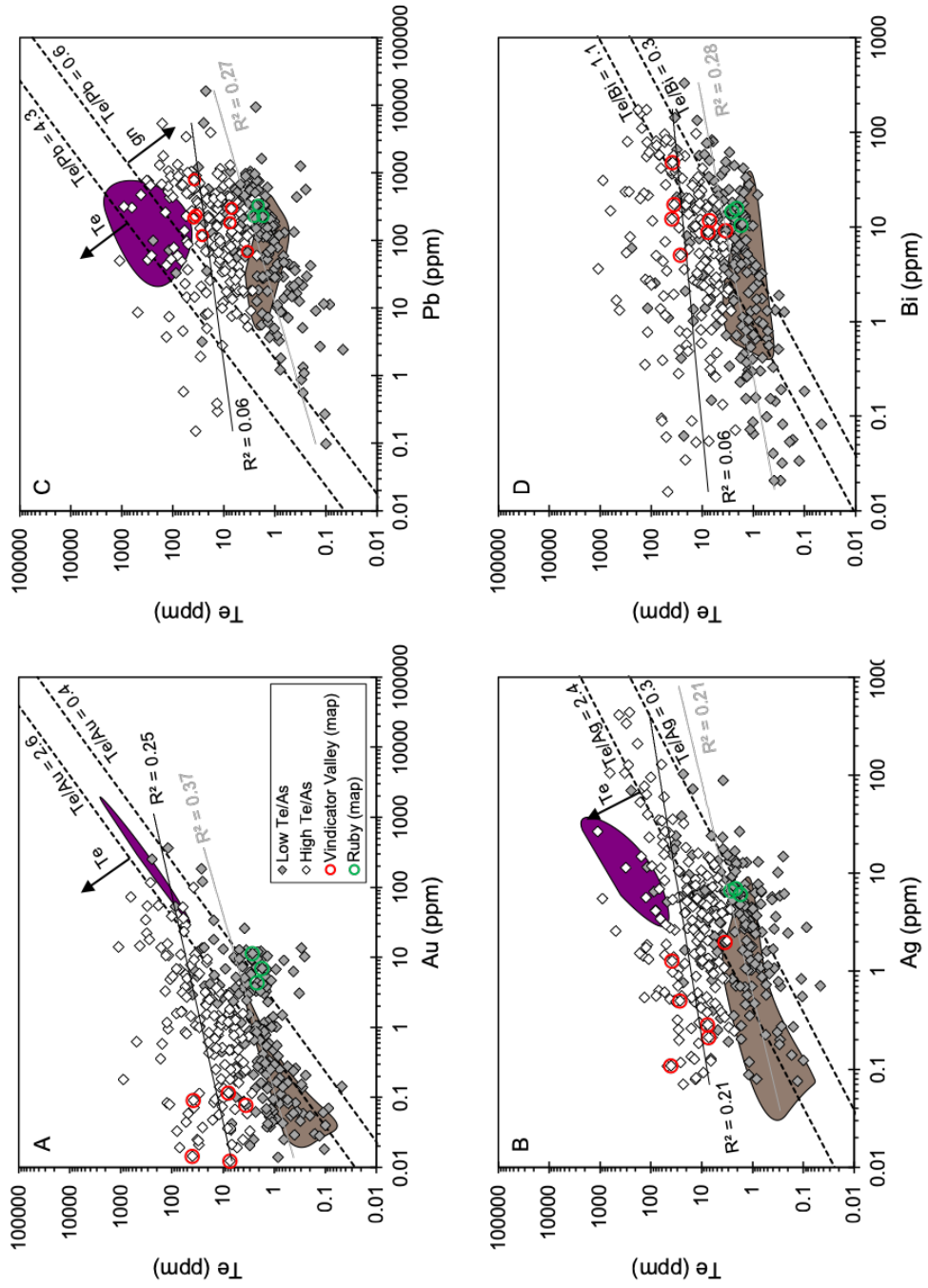
A
B
C
D
Te (ppm)
Au (ppm)
Ag (ppm)
Pb (ppm)
Bi (ppm)
Low Te/As
High Te/As
Vindicator Valley (map)
Ruby (map)
Te/Au = 2.6
Te/Au = 0.4
R² = 0.25
R² = 0.37
Te/Ag = 2.4
Te/Ag = 0.3
R² = 0.21
R² = 0.21
Te/Pb = 4.3
Te/Pb = 0.6
R² = 0.27
R² = 0.06
Te/Bi = 1.1
Te/Bi = 0.3
R² = 0.28
R² = 0.06
Te
Te
Te
Te

Fig. 12

TIME
LOW-GRADE BMS ORES
HIGH-GRADE Au-Te ORES
DEPTH
Vapor condensation (Te)
Vindicator Valley
Boiling zone (Au)
Ruby
Vapor (Te)
Mixing with meteoric water
Magmatic influx (Au, Te)
Boiling zone (Te, Au)
Au
clv
col
100 µm
Meteoric water-dominated
Boiling (py core, Ruby): Au precipitation → Te vapor partitioning at 220 to 350°C, pH 7 to 8 and -25 to -35 logfO_2
Vapor condensation (py core, Vindicator Valley): Host rock interaction → Fe^{2+} oxidation → fluid fO_2 decrease → Te deposition → Te-Au decoupling
Sections 5.3 (and 5.4)
Transition
Magmatic volatile influx initiated (py rim): Increasing fO_2 (above -25 to -35 log fO_2) → Te affinity to vapor decreases → Te-Au coupling
Section 5.3 and 5.4
Magmatic-dominated
Meteoric water mixing: Structurally controlled fluid upflow → mixing with meteoric waters → temperature decrease (105 to 200°C)
Shallow boiling (<1000m): Lower temperature and higher fO_2 → inefficient vapor-liquid separation → coupled Te-Au deposition
Sections 5.4 and 5.5

Fig. 13

Site	Type		Co	Ni	Cu	Zn	Se	As	Mo	Ag ppm	Cd	Sb	Te	Au	Tl	Pb	Bi
Ruby (Cresson)	Bulk ore	Min.	2.50	1.05	4.14	17.1	0.70	78.9	3.30	0.69	0.14	1.78	0.96	0.46	4.07	5.54	0.78
	Low-grade	Max.	14.3	6.99	17.3	88.7	27.9	225	166	2.14	1.50	4.18	4.03	2.86	6.26	61.3	1.78
		GSD	1.86	2.40	1.66	1.69	7.47	1.47	3.88	1.54	2.99	1.39	1.78	2.58	1.23	2.22	1.80
	n=4	GM	5.21	2.12	9.07	38.0	3.64	110	25.5	1.09	0.51	3.05	2.30	1.12	4.92	20.0	1.18
	Bulk ore	Min.	<1.20	0.72	7.10	7.50	1.76	18.7	3.16	3.16	1.42	4.22	51.5	37.8	2.19	24.9	4.56
	High-grade	Max.	<1.20	1.83	36.4	156	34.6	126	677	34.1	2.43	116	2235	1694	9.51	501	4.56
		GSD		1.94	1.84	3.15	4.47	2.40	3.28	2.68	1.35	3.46	5.45	5.47	2.10	4.08	
	n=5	GM		1.14	15.2	32.2	7.07	55.50	179	7.36	1.72	31.4	248	187	4.83	132	4.56
	Pyrite	Min.	0.12	0.17	0.135	0.82	0.66	0.93	0.05	0.08	0.10	0.12	0.11	0.01	0.02	0.26	0.02
	Low-grade	Max.	1018	796	3580	368	67.2	17860	625	411	0.35	149	1110	73	28.3	16300	334
		GSD	7.42	5.75	5.23	3.20	2.30	8.72	10.1	4.78	1.56	4.96	5.32	6.44	3.66	6.00	6.48
	n=178	GM	47.5	26.6	44.8	3.61	7.75	516	3.73	4.27	0.21	7.65	5.44	1.74	0.61	122	5.43
	Pyrite	Min.	0.12	0.15	0.60	2.01	1.14	2.06	0.06	0.11	<0.05	0.12	15.1	0.06	0.02	0.15	0.02
	High-grade	Max.	229	80	3130	276	33.7	34100	40.2	439	<0.05	1006	493	362	22.7	5550	23.7
		GSD	9.82	4.15	6.55	7.70	2.07	5.33	8.04	6.31		9.39	2.42	7.24	8.53	9.87	5.88
	n=27	GM	12.9	2.09	224	30.4	10.5	1570	0.85	12.0		6.91	70.2	12.7	0.68	37.9	1.54
WHEX	Bulk ore	Min.	2.81	2.91	3.62	119	0.60	5.19	1.31	0.18	0.04	0.81	0.79	0.04	2.76	10.1	0.30
	Low-grade	Max.	13.0	40.0	110	3255	20.8	64.8	5.03	8.69	9.30	118	2.16	0.95	9.56	596	34.0
		GSD	1.88	3.10	3.69	3.92	4.37	3.23	2.43	3.88	11.8	5.87	1.43	4.38	1.83	6.95	7.76
	n=4	GM	6.95	8.54	11.3	414	2.50	13.1	3.90	0.86	0.90	3.93	1.36	0.26	5.49	72.7	2.46
	Pyrite	Min.	0.68	0.85	0.76	1.11	0.58	0.21	0.06	0.04	0.15	0.05	0.05	0.02	0.03	0.10	0.02
	Low-grade	Max.	4490	868	248.5	850	70.0	192	381	31.9	0.76	520	124	3.65	6.49	1350	174
		GSD	9.8	8.57	4.96	5.86	4.33	5.50	9.52	7.38	57.2	11.1	4.9	4.97	4.25	7.76	12.7
	n=104	GM	37.9	27.1	26.4	8.89	9.24	8.16	1.51	3.41	2.76	2.47	3.26	0.18	0.49	28.9	2.92
Vindicator Valley	Bulk ore	Min.	1.86	1.57	3.18	26.9	0.71	10.4	1.71	0.03	0.73	1.83	0.07	0.02	2.48	45.4	0.4
	Low-grade	Max.	5.96	1.57	5.31	265	1.7	45.1	636	1.25	1.68	8.49	0.64	0.25	6.01	132	2.97
		GSD	1.60		1.28	2.36	3.15	1.66	7.98	4.29	1.49	3.78	1.09	3.24	1.38	1.41	2.42
	n=4	GM	2.92	1.57	3.72	88.0	2.17	25.4	72.0	0.29	1.17	4.50	0.38	0.07	4.12	90.2	1.46
	Pyrite	Min.	0.06	0.06	0.42	1.04	0.70	0.87	0.00	0.07	0.15	0.12	0.09	0.01	0.02	5.40	0.02
	Low-grade	Max.	1490	298	1050	900	89.1	6850	1120	15.3	2.38	67.5	905	11.0	8.10	9500	110
		GSD	6.69	6.27	5.97	5.78	3.33	5.89	13.02	3.86	2.36	4.75	5.48	5.36	3.65	4.38	8.46
	n=117	GM	22.2	5.36	13.2	6.06	14.9	116	1.74	1.09	0.36	4.55	6.23	0.21	0.32	150	5.06

Abbreviations: GM = geometric mean, GSD = geometric standard deviation

Table 1